40th Fluid Dynamics Conference and Exhibit
28 June - 1 July 2010, Chicago, Illinois

AIAA 2010-4721

Boundary-Layer Transition Measurements in a Mach-6 Quiet Tunnel

Christopher A.C. Ward*, Bradley M. Wheaton*, Amanda Chou*,
Peter L. Gilbert*, Laura E. Steen*, and Steven P. Schneider†
School of Aeronautics and Astronautics, Purdue University, West Lafayette, IN 47907-1282

Non-intrusive pressure-sensor measurements were made in the wake of a 10.2-mm cylindrical roughness in the laminar nozzle-wall boundary layer of the BAM6QT. The existence of an instability near 21 kHz within the wake was verified. A second instability near 40–60 kHz appears to occur at lower Reynolds numbers, and its frequency varies greatly with Reynolds number. Roughness dots were placed on a 3-m-circular-arc flared cone with a nearly sharp nosetip in an attempt to control streamwise vorticity. This streamwise vorticity is likely to be caused by an interaction between Görtler vortices and second mode waves. Roughness dots placed upstream of the temperature-sensitive paint showed no effect on the spacing of the vortices. Roughness dots placed directly on the temperature-sensitive paint altered the azimuthal spacing of the vortices to match that of the roughness dots. In an effort to investigate the effect of surface roughness on the crossflow instability, a 7-deg. half-angle cone was tested at 6-deg. angle of attack with temperature-sensitive paint. The average distributed surface roughness of the nosetip was varied by an order of magnitude. This did not have a significant effect on the crossflow instability, probably because of the residual forward-facing step at the leadinge edge of the paint. Heat-transfer measurements were made at the stagnation point of a hemispherical model to observe the effect of freestream noise; no effect was evident. The quiet nozzle throat was opened twice in April, after which a much-reduced maximum quiet pressure was observed. The throat is being recleaned and repolished in an effort to restore previous performance.

Nomenclature

α	thermal diffusivity
c_p	specific heat capacity
δ	boundary layer thickness
D	diameter (in.)
f	frequency (kHz)
k	roughness height
H	Enthalpy
M	Mach number
N	integrated amplification factor
n	azimuthal spacing
p	pressure (psia)
ρ	density
$\dot{q}$	heat flux
Re	Reynolds number
St	Stanton number
T	Temperature (°C or K)
t	time (seconds)
u	velocity
μ	viscosity
x	cone axial coordinate (m or cm)
y	cone spanwise coordinate (m or cm)
z	tunnel axial coordinate (in.)

Subscripts

0	stagnation condition
∞	freestream condition
D	based on diameter
e	edge condition
k	based on roughness height
i	initial condition
w	wall condition

*Research Assistant. Student Member, AIAA
†Professor. Associate Fellow, AIAA

Superscripts
′ fluctuations

Abbreviations
BAM6QT Boeing/AFOSR Mach 6 Quiet Tunnel
PSD Power Spectral Density
TSP Temperature-Sensitive Paint

I. Introduction

Laminar-turbulent transition in hypersonic boundary layers is important for prediction and control of heat transfer, skin friction, and other boundary layer properties. Vehicles that spend extended periods at hypersonic speeds may be critically affected by the uncertainties in transition prediction, depending on their Reynolds numbers. However, the mechanisms leading to transition are still poorly understood, even in low-noise environments.

Over the past 50 years, many transition experiments have been conducted in conventional ground test facilities.[1] However, these experiments are contaminated by noise radiating from the turbulent boundary layer typically present on the walls of the wind tunnel.[2] These noise levels (defined as root-mean-square of the pitot pressure fluctuations normalized by the stagnation pressure) are around 0.5-4% and an order of magnitude larger than seen under flight conditions.[3,4] These high noise levels can cause boundary layer transition to occur an order of magnitude earlier than in flight.[2,4] In addition, the mechanisms of transition operational in small-disturbance environments can be changed or bypassed altogether in high-noise environments; these changes in the mechanisms change the parametric trends in transition.[3] Therefore mechanism-based prediction methods must be developed and supported in part with measurements of these mechanisms in quiet environments.

I.A. The Boeing/AFOSR Mach-6 Quiet Tunnel

The Boeing/AFOSR Mach-6 Quiet Tunnel (BAM6QT) is presently the larger of two operational hypersonic quiet tunnels. It is designed as a Ludweig tube to minimize cost and provide high-Reynolds number quiet flow. A Ludweig tube is a long pipe with a converging-diverging nozzle on the end, from which flow exits into the nozzle, test section and a second throat (shown in Figure 1). To initiate Mach 6 flow, a diaphragm downstream of the test section is burst, causing an expansion wave to travel upstream through the test section into the driver tube. This expansion wave reflects between the upstream end of the driver tube and the contraction. A sufficient vacuum can extend the useful run time to many cycles of this expansion wave reflection (one cycle lasts roughly 200 milliseconds), where the stagnation pressure drops quasi-statically.

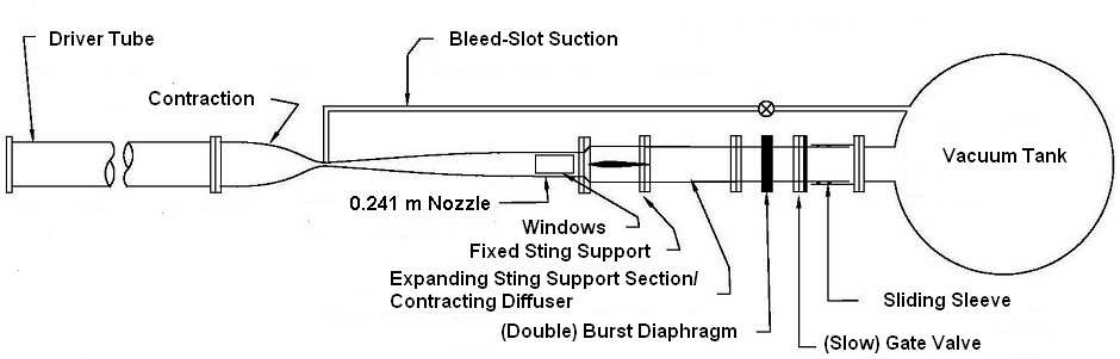

Figure 1. Schematic of Boeing/AFOSR Mach-6 Quiet Tunnel

The BAM6QT is capable of producing low noise levels on the order of 0.05% and employs several features to achieve this. A suction slot is present upstream of the throat and removes the boundary layer on the contraction wall, allowing a new undisturbed laminar boundary layer to grow on the nozzle wall. This suction slot is connected to the vacuum tank through a fast valve. This fast valve can be closed to produce noise

levels on the order of 3%, similar to conventional hypersonic tunnels. The tunnel also features a long nozzle designed to reduce the growth of Görtler vortices, a highly polished throat and nozzle, and high-quality air filters to reduce air-borne particulate in the tunnel.

II. Non-Intrusive Instability Measurements in the Wake of a 10.2-mm Cylindrical Roughness

II.A. Introduction

Among the many factors that can influence hypersonic transition is surface roughness. Roughness on the surface of a reentry vehicle can cause early transition and higher heating in flight.[5] Research is needed to determine if a naturally-occurring roughness will cause transition during reentry, or to determine the largest roughness that will begin to affect the natural transition location. Ideally, the growth of roughness-induced instabilities would be used to predict the location of transition.[6] A semi-empirical transition prediction method such as the e^N method might be used to reduce uncertainty in the location of transition induced by isolated roughness on hypersonic vehicles. However, these computational methods must be developed and validated with experimental measurements.

Measurements of an instability in the wake of a cylindrical roughness element have been made in the laminar nozzle-wall boundary layer of the Boeing/AFOSR Mach-6 Quiet Tunnel.[7–9] The instability was detected at a frequency near 21 kHz. This is believed to be the first detection of a roughness-induced instability at hypersonic speeds. Until now, stray effects that could cause an apparent instability were not fully ruled out. The largest concern remained a complicated shock/boundary-layer interaction caused by the hot-wire and pitot probes. To verify that the instability was real, non-intrusive flow measurements were taken and are reported here.

II.B. Non-Intrusive Pressure Measurements in the Roughness Wake

Non-intrusive measurements using flush-mounted pressure transducers on the nozzle wall were made at conditions similar to those used in previous measurements of the instability.[9] The pressure sensors were installed in inserts along the nozzle wall of the Mach-6 Quiet Tunnel, within the wake of the roughness. When operating with a laminar boundary layer on the nozzle wall, evidence of the previously-observed instability near 21 kHz was seen, as well as a new instability that occurs at lower Reynolds numbers.

II.B.1. Apparatus for Pressure-Sensor Measurements

Figure 2(a) shows the small window insert with the cylindrical roughness element.[9] A 5.97-mm-diameter micrometer head was used as a roughness element. For these measurements, the adjustable height of the roughness was left at a constant 10.2 mm. The micrometer was installed in a small circular insert at a tunnel axial coordinate of $z = 75.749$ in. Because all measurements are taken on the tunnel centerline, various inserts allow the spanwise position of the roughness to be changed between 0.0, 0.5, 1.0, 1.5, and 2.0 diameters off the tunnel center plane.

The window insert containing the roughness was modified in order to mount pressure sensors. A second circular insert was installed on the downstream end of the window (Figure 2(a)). The second circular insert contains five locations for mounting pressure sensors (three on the tunnel centerline and two off the tunnel centerline). Another insert containing pressure sensors was installed in the slot normally used by the traverse system for inserting probes into the tunnel.

All inserts were installed on the upper wall of the nozzle. Figure 2(b) shows a photograph of the entire apparatus, looking upstream through the end of the nozzle. The roughness is visible as a thin white line near the upstream end of the photograph. In this photograph, the roughness was placed two diameters off the tunnel centerline. Pressure sensors were mounted in both the circular insert as well as the traverse slot insert, and all sensors were installed on the tunnel centerline. A hot-film array was installed on the side wall of the nozzle and was used during each run to verify that the incoming boundary layer was laminar. Because the hot-film array was offset 90° from the roughness, it was not expected to interfere with the measurements.

Two types of pressure transducers were used: Kulite XCQ-062-15A and PCB 132A31. The Kulite XCQ-062-15A is a piezoelectric sensor with a 0.066-in. diameter, range of 0–15 psia, and a resonance frequency near 300 kHz. The Kulites are DC sensors, so both mean and fluctuation levels can be recorded. Both A-

and B-screens were used on the sensors. The A-screen has a flat dynamic response up to 30–40% of the resonance frequency while the B-screen response is flat only to 20% of the resonance frequency.[10] Further testing is needed to characterize the exact frequency response of these sensors. The PCB 132A31 has a resonance frequency above 1 MHz, with a minimum cutoff at 11 kHz. Thus, the PCB does not record mean pressure. The PCB has a larger diameter of 0.125 in. A summary of the installed sensors appears in Table 1. Unfortunately, the PCB at $z = 80.29$ in. suffered from leakage and was removed after only one run. All sensors were sampled using Tektronix oscilloscopes in High-Res mode at 2.0 MHz.

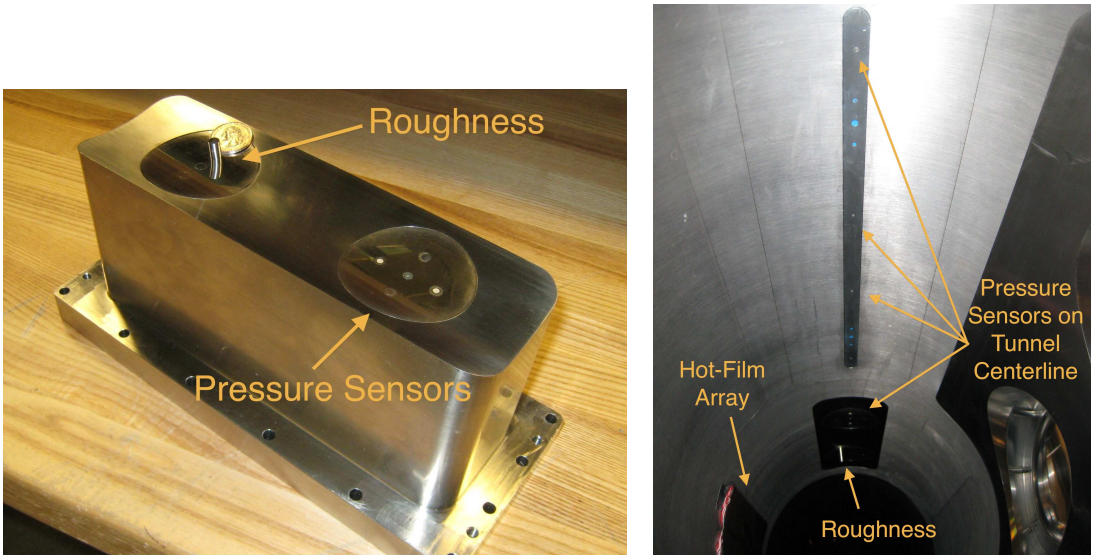

(a) Small window with roughness and pressure sensors (b) View looking upstream through nozzle

Figure 2. Window insert and photograph of the apparatus, looking upstream through the end of the nozzle. All pressure sensors were installed in inserts on the tunnel centerline. The roughness was moved off the tunnel centerline in order to make measurements off the center of the wake.

Table 1. Summary of sensors installed on the tunnel centerline. The PCB 132A31 at $z = 80.29$ in. was removed after one run due to leaking problems. The roughness was located at $z = 75.749$ in.

Tunnel Axial Location, z (in.)	Diameters Downstream from Roughness Edge	Sensor Type	Screen	Insert
80.29	18.8	PCB	-	Circular
80.89	21.4	Kulite	B	Circular
90.64	62.8	Kulite	B	Traverse Slot
93.64	75.6	Kulite	A	Traverse Slot
97.64	92.6	Kulite	A	Traverse Slot

II.B.2. Flow Conditions

Three Reynolds numbers were chosen for comparison to computations being performed at the University of Minnesota.[11] A summary of the three flow conditions appears in Table 2. Each run began at a different initial stagnation pressure ($p_{0,i}$) and a stagnation temperature of 433 K. All data appearing here were taken from t =1.0–1.2 s during the run, at which the stagnation pressure (p_0) is slightly lower than the initial value. Properties for the incoming laminar boundary layer were calculated using the Harris code.[12] M_e is the edge Mach number, Re_∞ is the freestream unit Reynolds number, k is the roughness height, δ is the boundary-layer thickness (defined as 99.5% of the freestream velocity), and Re_k is the Reynolds number based on roughness height k and conditions in the undisturbed laminar boundary layer at the height k.

Table 2. Test conditions.

Description	$p_{0,i}$ **(psia)**	p_0 **(psia)**	M_e	Re_∞ **(/ft)**	k/δ	Re_k
High Re	90	84	5.93	2.00×10^6	1.16	65,000
Mid Re	75	70	5.93	1.65×10^6	1.06	50,000
Low Re	64	60	5.93	1.40×10^6	0.98	30,000

II.B.3. Pressure-Fluctuation Amplitudes Remain Uncertain

Both the A-screen and B-screen Kulites were calibrated at low pressures between 0.03–0.40 psia while installed in the tunnel. However, at higher frequencies the amplitudes of the pressure fluctuations were different between the A-screen and B-screen sensors. To illustrate the difference, tests were performed with both a laminar and turbulent nozzle-wall boundary layer, with no roughness installed in the tunnel. These tests are similar to those by Beresh et al.[10] in a supersonic turbulent boundary layer. For these smooth-wall tests, Figure 3 shows a power spectral density plot of both A- and B-screen Kulites at various locations under laminar and turbulent flow. The large peaks near 300 kHz are from sensor resonance. Under laminar flow, the sensors are not excited and the amplitudes agree reasonably well except near 0.5–3.0 kHz. However, when the sensors are excited under turbulent flow the B-screen amplitudes begin to roll off at a frequency near 5–10 kHz. This is much lower than expected. The A-screen frequency response remains flat up to 50 kHz. The sensors exhibit response up to 100 kHz, but the actual amplitudes remain uncertain. The PCB amplitudes also remain uncertain, as the factory calibrations were used.

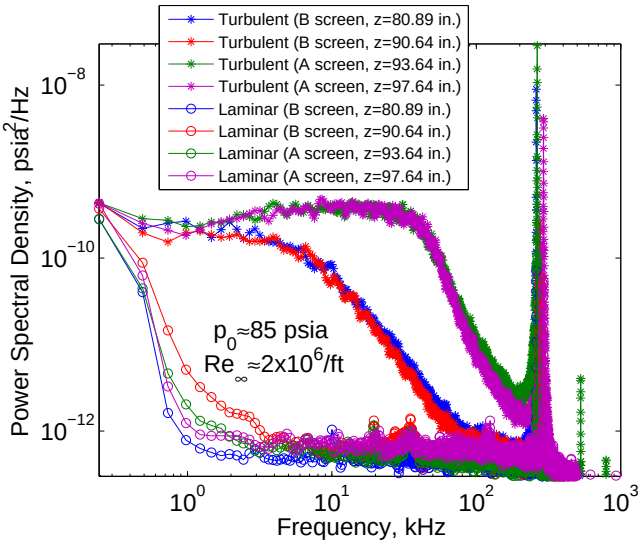

Figure 3. Smooth-wall spectra of both A- and B-screen Kulites, measuring laminar and turbulent boundary layers. The A-screen exhibits flat frequency response to 50 kHz while the B-screen rolls off near 5–10 kHz.

II.B.4. Instability near 21 kHz Verified on both Kulite and PCB Sensors

An initial test was performed to verify the existence of the instability near 21 kHz, observed previously with a probe intruding into the flow.[9] In the test, the pressure sensors were measuring 2.0 diameters off the wake centerline. No probe was present in the flow and the sensors were flush to the nozzle wall. A PCB and B-screen Kulite were used at similar locations (19 and 21 diameters downstream, respectively). The flow conditions were near the "High Reynolds number" case, similar to the conditions where the 21-kHz instability was observed before.

Figure 4 shows mean-square spectra of the pressure fluctuations at the wall. The frequency spacing for this and all mean-square spectra in this section was 0.25 kHz. The pressure-fluctuation amplitudes were nondimensionalized by the mean pressure at the wall. Both the Kulite and PCB show a large peak at 22 kHz. This peak is the instability that has been observed previously using hot-wire and pitot probes.

Several harmonics are also seen. The detection of the instability with non-intrusive flow measurement techniques confirms its existence. However, the amplitudes of the fluctuations differ between sensors by an order of magnitude, for unknown reasons. The PCB factory calibration was used, and the mean pressure from the Kulite was used to nondimensionalize both pressure-fluctuation amplitudes. The Kulite has a B-screen, which may have significantly lowered the fluctuation levels above 5–10 kHz.

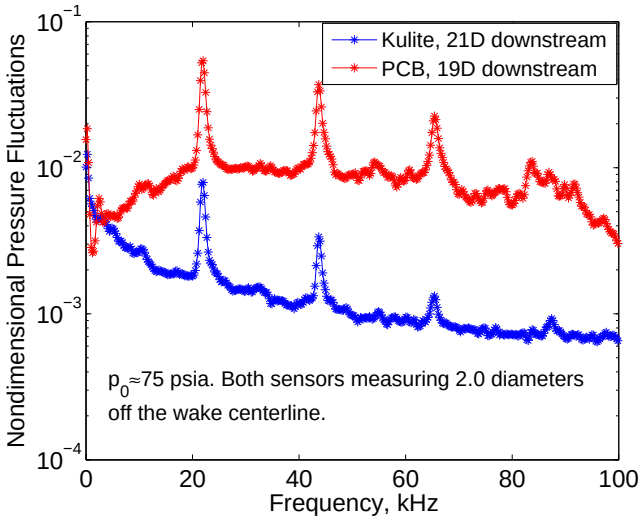

Figure 4. Detection of the 21-kHz instability in the absence of a probe in the flow. The amplitudes differ by an order of magnitude for unknown reasons. Several harmonics are seen in the spectra. Pressure fluctuations nondimensionalized by the mean pressure, as measured experimentally by the Kulite.

II.B.5. High Reynolds Number Case: Instability near 21 kHz Breaks Down Closer to Roughness

The PCB was removed after one run due to leaking problems and the four Kulites were used to examine the wake of the roughness. At the High Reynolds number, the 21-kHz instability was observed only on the closest sensor (21 diameters downstream from the roughness). The three downstream sensors showed fully turbulent flow. Mean-squared spectra of the sensors at various spanwise positions in the wake are shown in Figure 5, along with smooth-wall laminar and turbulent spectra. At 21 diameters downstream, the flow is turbulent with a large peak near 21 kHz and several harmonics. The peaks are strongest off the wake centerline (Figure 6). At the second sensor and beyond, the flow appears to be fully turbulent and the instability peaks disappear (Figure 5(b)).

II.B.6. Middle Reynolds Number Case: Flow Breaks Down over a Longer Distance

Spectra at the middle Reynolds number are shown in Figure 7 for the three sensors closest to the roughness. At 21 diameters downstream of the roughness, the fluctuation amplitudes are lower overall than at the high Reynolds number. The instability near 21 kHz is still visible with multiple harmonics. Farther downstream, the flow appears transitional with additional peaks that may be other instabilities. At the third sensor (76 diameters downstream), the flow appears fully turbulent. The shape of the turbulent spectra, as well as the fluctuation amplitudes, are different for the third sensor because the A-screen was used instead of the B-screen. The flow develops and transitions over a longer area than at the higher Reynolds number, as would be expected.

II.B.7. Low Reynolds Number Case: New Instability near 40–60 kHz Seen and Flow Breaks Down over Range of All Sensors

At the lowest Reynolds number, the instability near 21 kHz is not seen (Figure 8). Instead, a new instability appears at a higher frequency of 40–60 kHz. The flow is more laminar nearer to the roughness and the transition process appears to occur over the length of all four sensors. At 21 and 63 diameters downstream, a narrow instability peak is seen near 55 kHz in a nearly-laminar wake. At 76 diameters downstream the

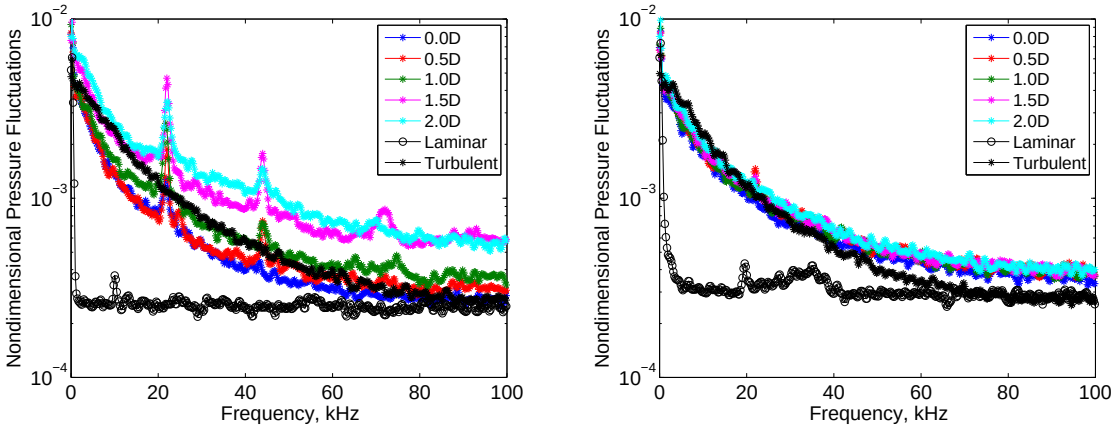

(a) 21D Downstream (Kulite B Screen)

(b) 63D Downstream (Kulite B Screen)

Figure 5. High Reynolds number case. The instability near 21 kHz was observed only at the closest sensor. Farther downstream, the flow was turbulent. Legend denotes the number of spanwise diameters (D) off the wake centerline. Pressure fluctuations nondimensionalized by the mean pressure at the wall. Smooth-wall laminar and turbulent traces are shown for comparison.

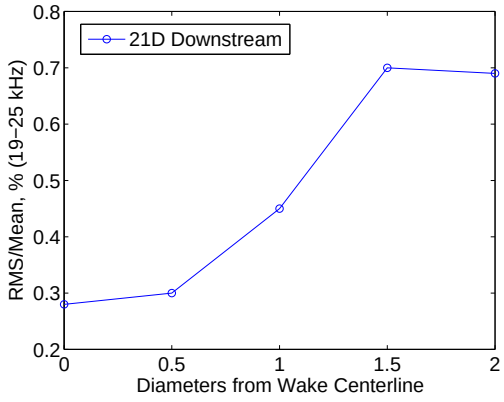

Figure 6. Spanwise strength of the fluctuations from 19–25 kHz, calculated by integrating the area under the power spectrum and nondimensionalized by the mean pressure.

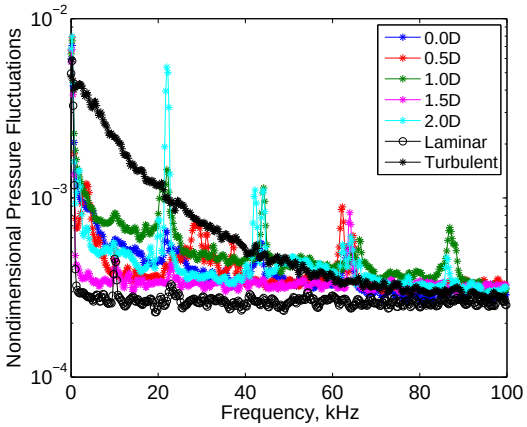

(a) 21D Downstream (Kulite B Screen)

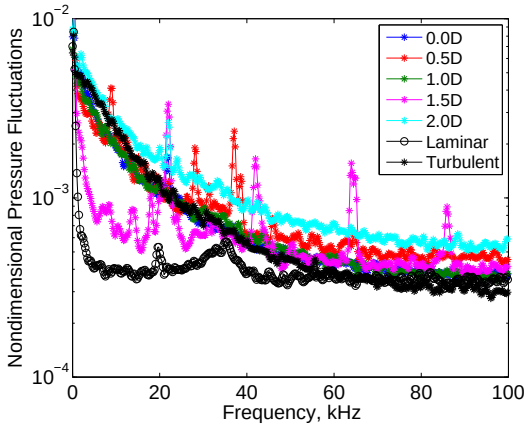

(b) 63D Downstream (Kulite B Screen)

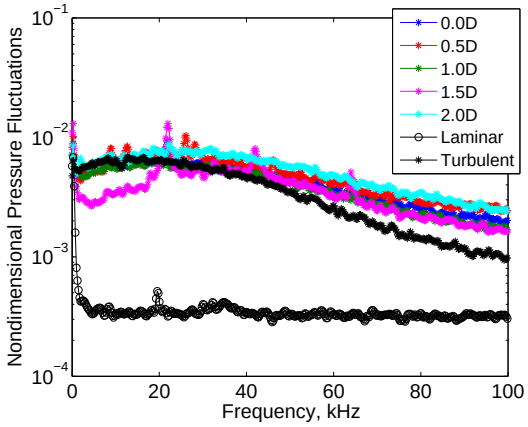

(c) 76D Downstream (Kulite A Screen)

Figure 7. Middle Reynolds number case. The flow breaks down over a longer distance, but the instability near 21 kHz is still seen. Legend denotes the number of spanwise diameters (D) off the wake centerline. Pressure fluctuations nondimensionalized by the mean pressure at the wall. Smooth-wall laminar and turbulent traces are shown for comparison.

wake becomes transitional with higher fluctuation levels. In addition, the 55-kHz peak begins to broaden. At 93 diameters downstream the flow is near fully turbulent. The frequency of the new instability was not observed to change significantly with downstream distance. It is possible that an entirely different type of instability is responsible for transition when the roughness is "submerged" within the boundary layer.

Unlike the 21-kHz instability, this new instability appears to be highly dependent on Reynolds number. Figure 9(a) shows spectra from the closest sensor during a single run with $p_{0,i} = 64$ psia, measuring 2.0 diameters off the wake centerline. Each spectra is from a different time during the run, corresponding to a different Reynolds number. The peak frequency decreases roughly 20–25% as the freestream unit Reynolds number decreases by 10%. The instability frequency has been observed to vary almost linearly with freestream Reynolds number over a small range. Figure 9(b) shows the instability frequency versus Reynolds number for several runs with different initial stagnation pressures. The measurements were taken at various positions within the wake using both wall sensors and a pitot probe. The frequencies are close between different runs, but do not match up exactly. Several assumptions made when calculating Reynolds number could cause this difference (mainly the viscosity).

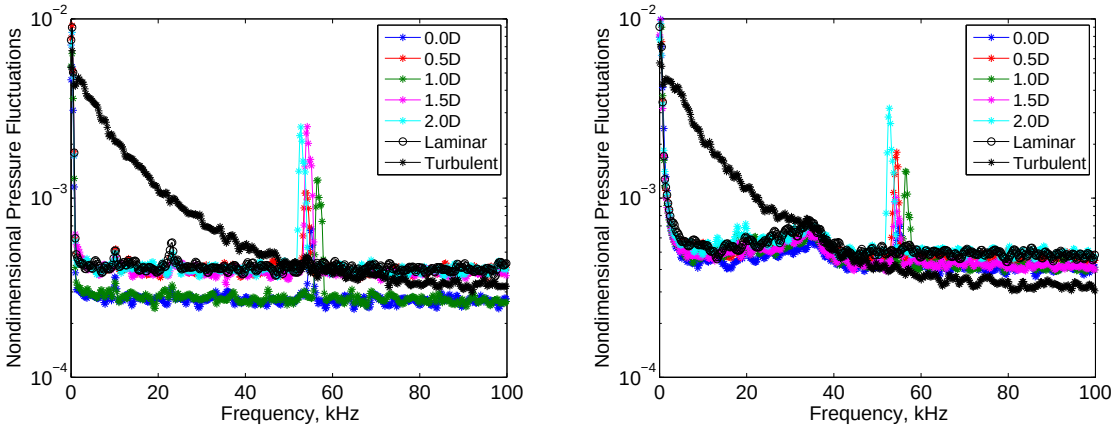

(a) 21D Downstream (Kulite B Screen)

(b) 63D Downstream (Kulite B Screen)

(c) 76D Downstream (Kulite A Screen)

(d) 93D Downstream (Kulite A Screen)

Figure 8. Low Reynolds number case. Legend denotes the number of spanwise diameters (D) off the wake centerline. Pressure fluctuations nondimensionalized by the mean pressure at the wall. Smooth-wall laminar and turbulent traces are shown for comparison.

II.C. Summary

Efforts are ongoing to make detailed measurements of instabilities within the wake of a cylindrical roughness in the laminar nozzle-wall boundary of the BAM6QT. Non-intrusive measurements have verified the instability near 21 kHz previously reported in References 7–9. This is the first measurement of an instability behind an isolated roughness in a laminar boundary layer at hypersonic speeds. The measurements were

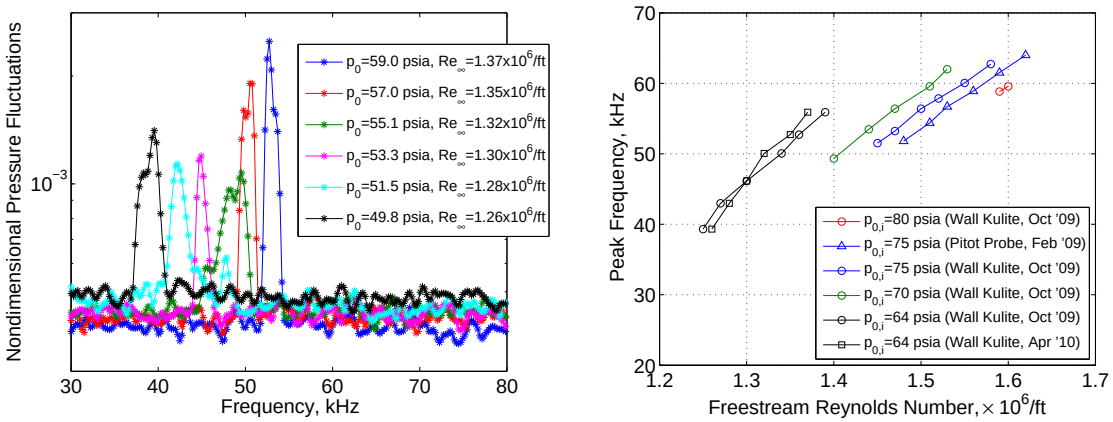

(a) Spectra from B-screen Kulite at 21D downstream and 2.0D off the wake centerline. Single run with decreasing Reynolds number.

(b) Instability frequency vs. Reynolds number. Multiple runs with different initial stagnation pressures. Both wall Kulites and pitot probe were used.

Figure 9. Frequency-dependency of the higher-frequency instability near the "Low Reynolds number" condition.

made with flush-mounted wall pressure sensors; however, the fluctuation amplitudes of the sensors still need improved calibrations.

Measurements in the wake of a 10.2-mm roughness were made at three different Reynolds numbers. It appears that two separate types of instabilities were detected:

1. The first instability near 21 kHz occurs at Re_k near 50,000–70,000 and $k/\delta \approx 1.1$–1.2. This instability breaks down less than 20 diameters downstream of the roughness and requires more instrumentation closer to the roughness. Its frequency varies only slightly with freestream Reynolds number.[9]

2. The second instability occurs at higher frequencies of 40–60 kHz. Its frequency appears to vary greatly with freestream Reynolds number. The second instability occurs at Re_k near 20,000–30,000 and $k/\delta \approx$ 0.9–1.0. This instability breaks down farther from the roughness (greater than 60 diameters downstream) and would require additional instrumentation farther from the roughness.

Future work will involve characterizing the Reynolds number ranges for which each type of instability appears. Both the roughness height and freestream Reynolds number can be changed in future experiments. A new insert could be manufactured with pressure sensors at more locations. Because each case needs to be instrumented differently, it should be decided which type of instability is more applicable to real design problems. Computations should then be performed by others for the most desired case, and compared to detailed measurements with wall sensors and probes.

III. Effect of Tunnel Noise on Laminar Stagnation-Point Heating at Mach 6

III.A. Background

For hypersonic flight vehicles, thermal management is a dominant design concern. Several studies on blunt re-entry vehicles have found increases in heating near the stagnation region that are not predicted by computational analyses. This heating augmentation has been seen in a number of facilities over a wide range of test conditions [13,14,15]. One potential cause of this stagnation-region heating augmentation is tunnel noise. In order to characterize the effect of tunnel noise, heat-flux measurements were made for similar blunt geometries in quiet and noisy conditions using the unique features of the BAM6QT.

III.B. Models and Experimental Setup

Three 15-5 H1100 stainless-steel models were provided by AEDC Tunnel 9 for testing in the BAM6QT. A 1.414-in.-diameter calibration hemisphere was fitted with seven 0.125-in.-diameter Schmidt-Boelter heat-flux gages on a centerline at intervals of 30°, with one at the stagnation point. A second, 1.5-in.-diameter

hemisphere was fitted with seven 0.0625-in.-diameter type-E coaxial thermocouples. The smaller-diameter coaxial thermocouples provide higher spatial resolution than the larger Schmidt-Boelter gages. A beaded thermocouple was attached to the inside surface for base temperature measurements. Comparisons were made between the different measurement techniques used for each hemisphere.

Tests were also conducted using a 1.5-in.-diameter model of the CEV forebody heat shield (Figure 10). Seven 0.03125-in.-diameter type-E coaxial thermocouples were mounted along a centerline. The smaller thermocouples were used for the CEV model to enable increased spatial resolution for studies of the laminar heating augmentation effect. Since the stagnation region is of particular interest, five of the thermocouples were positioned within $\frac{x}{R} = \pm 0.25$ of the stagnation point, where R is the model radius and x is the distance from the model's geometric center.

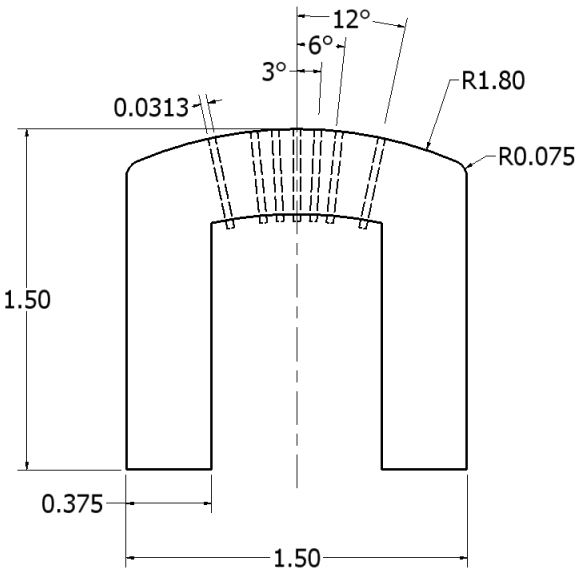

Figure 10. Cutaway of the 1.5-in., 15-5 stainless-steel model of the CEV forebody heat shield. Dimensions in inches.

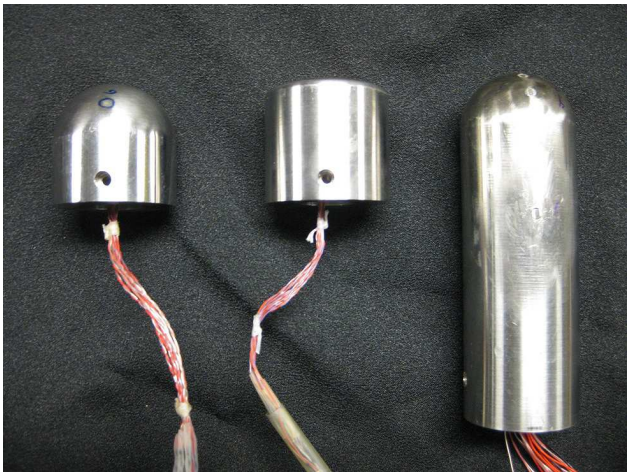

Figure 11. Coaxial-thermocouple hemisphere, CEV forebody, and Schmidt-Boelter hemisphere (from left to right)

Stagnation point sensors were amplified by a gain of 100 and low-pass filtered at 30 Hz prior to acquisition using a Stanford Research Systems SR560 Low-Noise Preamplifier. The stagnation pressure during each run was obtained using an XTEL-190-200A Kulite pressure transducer mounted at the entrance to the tunnel contraction. Stagnation temperature is found using hot-wire techniques with a constant-current anemometer (CCA). The hot wire was positioned in the free-stream flow 2 inches above the model, at the same axial

location as the model stagnation point. An uncalibrated Senflex hot-film array mounted on the nozzle wall was used as a qualitative measure of flow quality. Data were recorded using two model DPO7054, a TDS7104, and a TDS5034B Tektronix digital oscilloscope. Data for all thermal sensors were sampled at 5 kHz for 10 sec per run in high-resolution mode.

III.C. Computational Methods

III.C.1. Numerical Heat Equation Solver

While Schmidt-Boelter gages are able to make direct measurements of heat flux, additional steps must be taken to obtain heat-transfer rates from thermocouple temperature data. The one-dimensional, unsteady heat conduction equation in spherical coordinates, given in Eq. 1, is solved numerically using the AEDC Matlab code, `QCALC96`.

$$\frac{1}{\alpha}\frac{\partial T}{\partial t} = \frac{1}{r}\frac{\partial T}{\partial r} + \frac{\partial^2 T}{\partial r^2} \tag{1}$$

Thermal diffusivity, $\alpha = k/\rho c_p$, is dependent on the thermal conductivity, k, density, ρ, and the specific heat capacity, c_p, of the wall material. A wall temperature gradient is found and used along with Fourier's law to find the wall heat flux.

The code uses temperature and time vector input arguments in a second-order, Euler-explicit finite difference approximation of a homogeneous, finite-thickness slab. This code is a modified version of the original `QCALC` Fortran code, developed by Boyd and Howell.[16] Uniform initial temperature is assumed throughout the slab, with the front-face boundary condition measured by a coaxial thermocouple. The back-face boundary can either be measured by a surface-mounted beaded thermocouple or be assumed adiabatic. In general the adiabatic assumption is used, as heating due to the increase in back-face temperature during a run was found to be insignificant. The finite difference method utilizes evenly spaced nodes through the thickness of the model wall. The number of nodes is determined by a stability parameter based on the size of the input time vector and material properties. The spatial loop is nested within a time loop, which updates and stores nodal temperatures for use in the second-order finite difference method to acquire the wall temperature gradient.

Temperature-dependent functions are used for thermal conductivity and specific heat of the wall material. Though it would be expected that Chromel thermal properties be used for thermocouple data, Coblish found the best agreement for a 15-5 stainless steel model fitted with Type-E coaxial thermocouples by using 17-4 stainless steel properties.[17] Material properties are taken from References 18 and 19.

III.D. Heating Measurements in Quiet and Noisy Flow

Stagnation-point heating measurements with coaxial thermocouples are presented in Figure 12 for noisy and quiet flow. Initial unit Reynolds number for the quiet run is 3.12×10^6/ft, with $T_{0,i} = 160$ °C, $p_{0,i} = 144$ psia, and initial wall temperature, $T_{w,i} = 30$ °C. Initial unit Reynolds number for the noisy run is 3.16×10^6/ft, with $T_{0,i} = 160$ °C, $P_{0,i} = 132$ psia, and $T_{w,i} = 27$ °C. At such low Reynolds numbers, the boundary layer over the model face is assumed to be entirely laminar. Initial Reynolds numbers are matched between quiet and noisy runs. Most of the thermocouple data were obtained near an initial unit Reynolds number of 3.15×10^6/ft, as this was near the maximum pressure at which clean, quiet flow could be achieved.

Measured heating is compared to predictions computed using an axisymmetric stagnation-point similarity equation solver, `CBLSS`. This program takes inputs of Mach number, stagnation pressure, stagnation temperature, model-wall temperature, and nose radius and outputs a predicted heating based on a similarity solution. Details for the computational method are available in Reference 20. `CBLSS` calculations are shown alongside experimental results in Figure 12. Theoretical slopes match those of the heating data, but computations are 2-7% higher than experimental data. Over the full range of test conditions for the thermocouple hemisphere, computed heating rates are 2-10% higher than measured heating rates.

Lower heating is to be expected from thermocouple measurements due to three-dimensional heating effects not accounted for in the one-dimensional `QCALC96` heating model. An ANSYS analysis of radial heating was conducted to determine expected losses in heating from the stagnation point of a hemisphere due to radial conduction. Two-dimensional heat conduction was modeled for a hemisphere by using a theoretical surface heating distribution normalized by the Fay-Riddell stagnation-point value. The analysis revealed about a

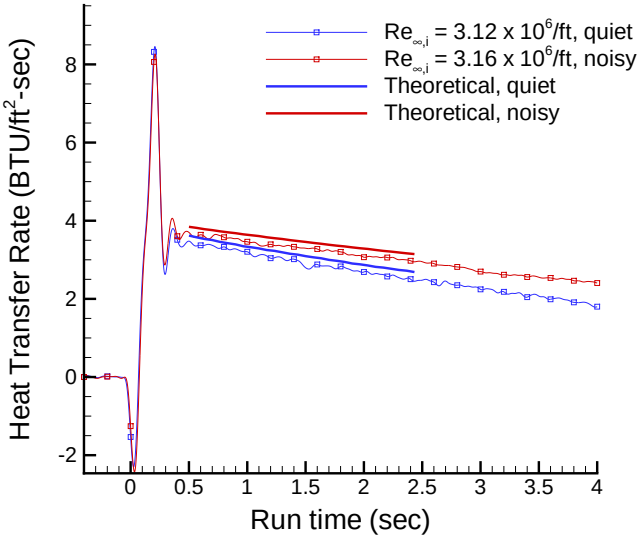

Figure 12. Comparison of stagnation heat-flux and computation time histories for the thermocouple hemisphere

$7-10\%$ heating loss at the stagnation point due to radial conduction. Similar heating losses were found for the same hemisphere radius regardless of the input heating level.[21]

Runs begin with a brief heating impulse during tunnel startup, seen as the spike near $t = 0$ sec. The quiet run ends after about 6 sec with an abrupt jump in heating due to the complex shock environment during shutdown. The noisy run ends later, after about $9-10$ sec. The decrease in stagnation pressure is faster in quiet flow due to higher mass flux from bleed-slot suction, hence a shorter run duration than in noisy flow. This also results in a larger Reynolds number range in a quiet-flow run for the same amount of run time.

The non-dimensional Stanton number, St, and Reynolds number based on nose diameter, $Re_{\infty,D}$, are therefore used for comparisons of quiet and noisy data. Since the change in Stanton number is nominally proportional to $1/\sqrt{Re_x}$ in the flat-plate case, the parameter given in Eq. 2 is roughly constant.[22]

$$St \times \left(\mathrm{Re}_{\infty,D}\right)^{1/2} = \frac{\dot{q}}{\rho_\infty u_\infty \left(H_0 - h_w\right)} \left(\frac{\rho_\infty u_\infty D}{\mu_\infty}\right)^{1/2} \tag{2}$$

$$H_0 - h_w = \left(c_p T_\infty + \frac{u_\infty^2}{2}\right) - c_p T_w$$

where $\dot{q}$ is the heat flux, ρ_∞ is the free-stream density, u_∞ is the free-stream velocity, μ_∞ is the free-stream dynamic viscosity, H_0 and h_w are the total and wall enthalpies, and c_p is the specific heat of air.

Non-dimensional heating is shown along with CBLSS computations in Figure 13. The data appear nearly constant over the Reynolds number range of the runs, with good agreement between the quiet and noisy cases. Figure 14 provides a comparison of the quiet and noisy cases through ratios of measured to theoretical Stanton parameters. The ratio of the experimental to theoretical Stanton parameter is shown as a function of free-stream unit Reynolds number. Experimental values for both quiet and noisy conditions fall within 7% of CBLSS predictions. Variation in Stanton parameter ratio between quiet and noisy flow is within the measurement accuracy, indicating no heating augmentation effect. Repeatability of results was found to be within $\pm 2.5\%$.

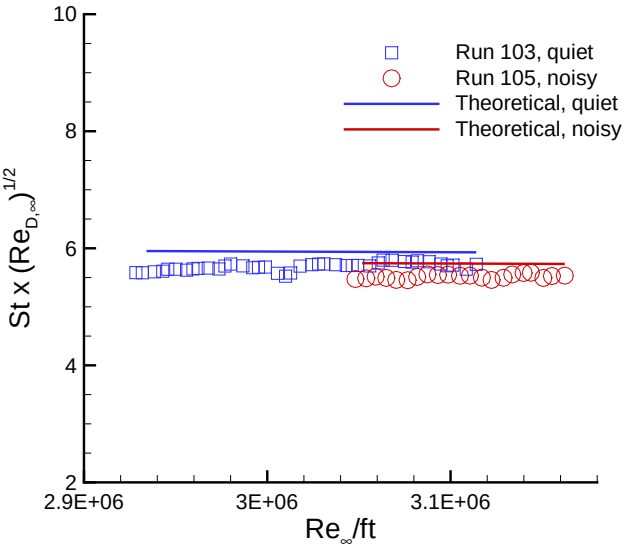

Figure 13. Heat flux transformed by the Stanton parameter near $Re_{\infty,i} = 3 \times 10^6$/ft for the thermocouple hemisphere

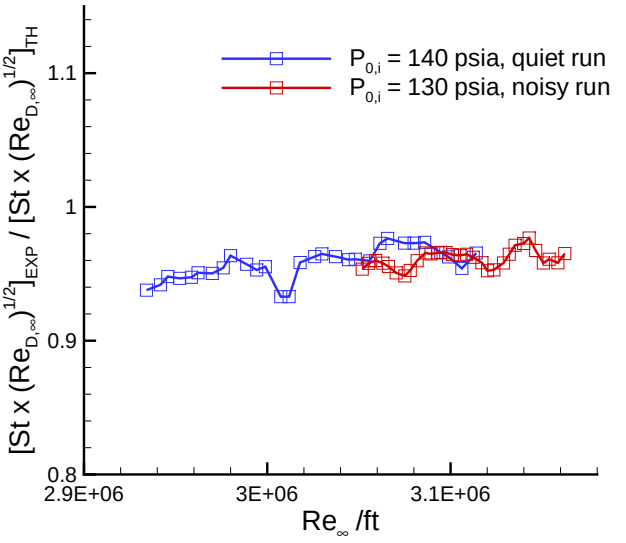

Figure 14. Comparison of quiet and noisy heating to theoretical values near $Re_{\infty,i} = 3 \times 10^6$/ft for the thermocouple hemisphere

III.D.1. Schmidt-Boelter Gage Hemisphere

Runs were conducted with the 1.414-in.-diameter hemisphere equipped with Schmidt-Boelter gages in quiet and noisy flow for unit Reynolds numbers between 1.8×10^6 and 2.8×10^6/ft. Non-dimensional results are shown in Figure 15(a) for runs near an initial stagnation pressure of 120 psi. While no data are presently available at matched Reynolds numbers, measured heating levels appear to agree between quiet and noisy conditions at matched initial stagnation pressures. Ratios of experimental to predicted Stanton parameter, plotted in Figure 15(b), show that any dependence on noise is within the measurement error.

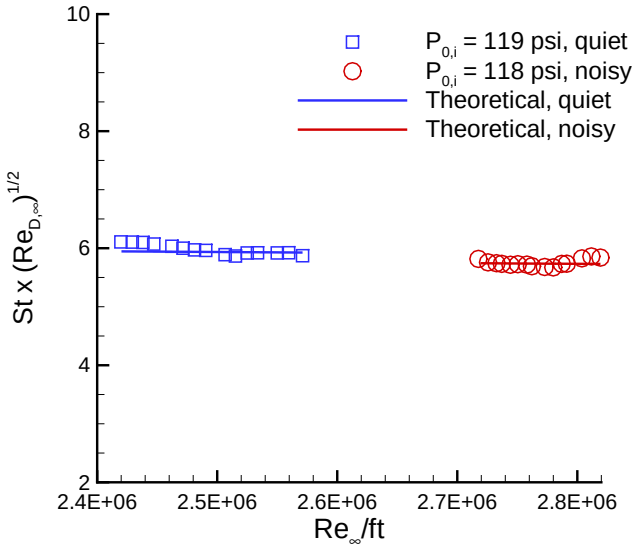

(a)

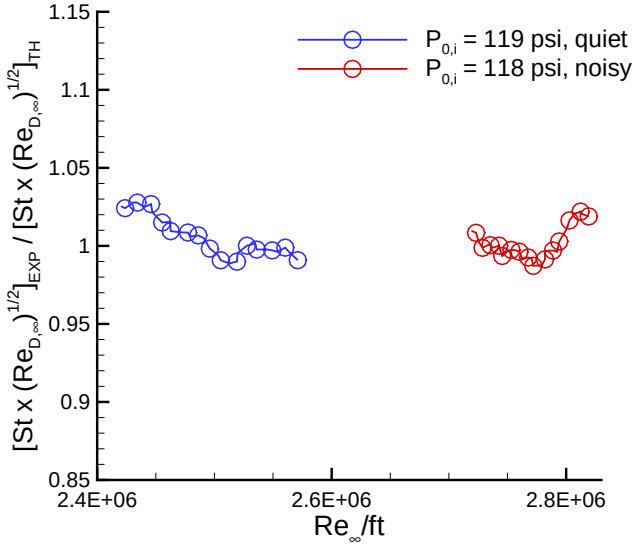

(b)

Figure 15. (a) Stanton parameter for quiet and noisy runs near $Re_{\infty,i} = 2.5 \times 10^6$/ft, (b) Ratios of Stanton parameter for runs with the Schmidt-Boelter hemisphere

It should be noted that Schmidt-Boelter measurements agree more closely with computations than the thermocouple data. This is expected since Schmidt-Boelter gages are direct heat-transfer transducers with nominally flat sensing surfaces. Thus, they are not affected by errors associated with the one-dimensional

heat equation solver and radial heat conduction. A comparison of Schmidt-Boelter and coaxial-thermocouple data is shown in Figure 16. Data are normalized by model nose radius, R_N, since stagnation-point heating is proportional to $1/\sqrt{R_N}$. There is good agreement between the two sensing methods once thermocouple data are corrected for the $\sim 7\%$ heating loss due to radial conduction.

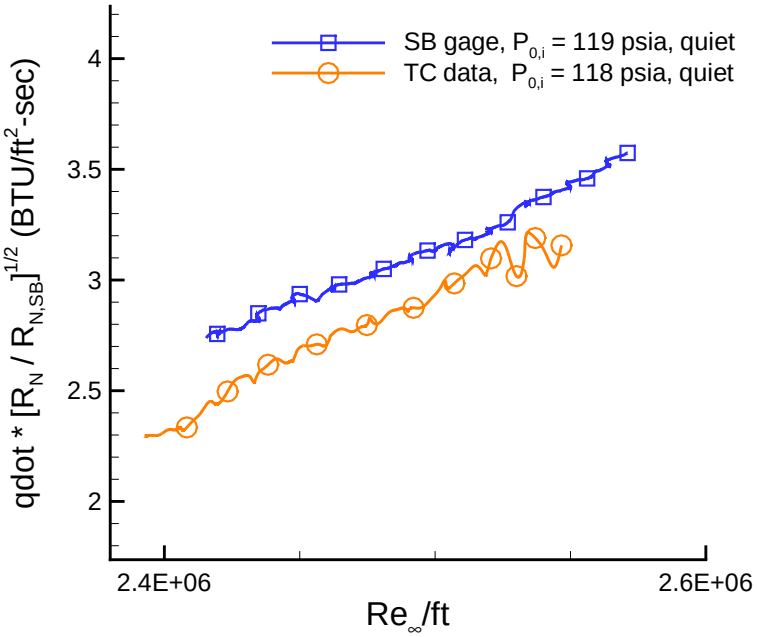

Figure 16. Comparison of thermocouple and Schmidt-Boelter data

III.E. CEV Forebody Heat Shield

Quiet and noisy-flow heating data with the 1.5-in. CEV model were desired for a comparison to similar CEV tests performed in AEDC Tunnel 9 and the NASA Langley 20-in. Mach-6 tunnel [13,23]. It is possible that a heating augmentation effect may be evident on the CEV model and not the hemisphere due to the larger subsonic region of the CEV. Several runs were conducted over a large range of Reynolds numbers, but the model did not start in noisy flow. Additional permutations of tunnel conditions to start the model remain to be tested. Measurements with a CEV model fitted with pressure instrumentation are needed to determine when this blunter model can be started.

III.F. Measurement and Computational Uncertainty

The largest source of error in the coaxial-thermocouple measurements is the one-dimensional assumption in the `QCALC96` analysis. As previously mentioned, heating losses due to radial heat conduction result in an uncertainty of up to $\pm 10\%$. The thermal properties used for the one-dimensional heat equation solution are an additional source of uncertainty. Since models are generally made from steel and type-E thermocouples are constantan and chromel, it is difficult to define the exact material properties to be used in the heat-flux analysis. Work at AEDC Tunnel 9 has determined that the combination of 17-4-H1150 stainless-steel properties with a 15-5-H1100 stainless-steel model provides the most accurate heating results. A $\pm 4\%$ uncertainty was found for these properties.[17]

Additional uncertainty is added by variations in free-stream conditions during runs in the BAM6QT. While no in-depth study has yet been conducted of the uncertainties for free-stream conditions in the BAM6QT, estimates are made here based on measurements performed. Scatter in pitot measurements used to obtain Mach number gives an uncertainty of $\pm 1.7\%$. Uncertainty due to cold-wire accuracy and end-loss heating is $\pm 4\%$. This gives an estimated free-stream condition uncertainty of $\pm 4.3\%$. Overall uncertainty

for the thermocouple hemisphere measurements, found as the root-square of the individual uncertainties, is ±11%.[24]

Nominal estimated heat-flux uncertainty for Schmidt-Boelter gages is ±5% of the measurement [25,21]. The additional tunnel-condition uncertainty in the BAM6QT of ±4.3% brings the overall uncertainty to ±6.5% for Schmidt-Boelter heating data.

While no direct validation has been performed for the `CBLSS` code, extensive testing has been done for the Fay-Riddell correlation, which agrees closely with `CBLSS`. The velocity gradient formulation used in the Fay-Riddell heat-flux calculation can result in uncertainties of up to ±10%. Good agreement with experiment, about ±2%, has been found for the modified Newtonian formulation in other studies.[26] The majority of the computational uncertainty in applying the code to the BAM6QT arises from uncertainties in knowledge of external flow properties. Small deviations in flow properties result in large deviations in computations.[27] Air properties from Lemmon's algorithm are known within ±2% for the flow conditions in the BAM6QT, though a conservative estimate of ±4% is used due to uncertainties in pressure and temperature measurements.[28] This results in uncertainties of ±0.5%, ±1.6%, and ±2% due to viscosity, specific heat, and thermal conductivity, respectively. A conservative overall uncertainty for the `CBLSS` computations is therefore ±5%.

IV. Tunnel Performance

The performance of the BAM6QT degraded in May 2010. The maximum quiet pressure decreased after the nozzle throat was opened to measure dimensions for a new throat. Previous maximum quiet and maximum intermittently-quiet pressures were reported in January.[29] Since April, the nozzle has been opened multiple times for measurements, and the maximum quiet pressure has decreased. Before the nozzle was opened, however, tests were run to determine characteristics of the airflow in the BAM6QT test section.

IV.A. Methods

An XCQ-062-15A Kulite pressure transducer was mounted into a pitot probe to measure the mean and fluctuating pressures near the nozzle exit. The root-mean-square (RMS) of the pressure fluctuations indicate the noise levels in the BAM6QT. High fluctuations due to sensor resonance could alter the RMS of the total signal. For this reason, the RMS is calculated by integrating the power spectra of the fluctuations not including the sensor resonance.

The power spectral densities are created by taking a 0.1-second segment of the measured pressure, subtracting the mean, and using Blackman windowing with 500 points in each segment, 50% overlap of each window, and averaging 1000 Fast-Fourier Transforms. The resonance frequency may vary by over 100 kHz for different sensors, and integrating to different frequency levels would cause additional discrepancies in RMS levels. Kulite quotes their pressure transducers as trustworthy to a frequency response up to one fifth their resonance frequency,[30] which is typically between 200 and 350 kHz. For these reasons it has been chosen to integrate all power spectra to 50 kHz. The square root of the integral gives the RMS, which is normalized by the mean pressure to give the noise level of the BAM6QT. Since previous noise-calculation measurements have been integrated to around 200 kHz, the current RMS levels are lower, on the order of 50%, of those reported in the past.

The DC-coupled voltage from the pressure transducer is used for all mean pressure values as well as for RMS calculations with a turbulent nozzle-wall boundary layer. For a laminar nozzle-wall boundary layer the fluctuations are much lower, and the AC-coupled voltage, amplified by an additional factor of 100, is used for greater resolution and accuracy in calculating RMS. AC-coupled voltages cannot be used with a turbulent nozzle-wall boundary layer because the amplifier clips.

Qualitative flow conditions can also be determined from a hot film array located on the nozzle wall. The hot films are uncalibrated and cannot give quantitative results, but they are also non-intrusive and can give information about flow characteristics (quiet, noisy, or separated) while a model is in the tunnel. RMS calculations are taken from the more-accurate pressure-transducer pitot probe.

IV.B. Mapping the Extent and Quality of Quiet Flow

It has been stated that "the critical performance parameter for a quiet tunnel is the Reynolds number based on freestream conditions and the length along the centerline of the region of uniform quiet flow Δx".[31]

The effect of axial variations in tunnel noise was explored at NASA Langley Research Center after the completion of the first successful quiet tunnel in 1984. Measurements were made on a sharp cone at two different axial locations, and results showed that transition in the low-disturbance tunnels was dominated by the local stream noise that was incident on the cone boundary layer near the nosetip.[32] This report also showed there was an axial variation in noise level in the nozzle, which resulted in a variation of transition location on the cone model.

The BAM6QT research group previously defined quiet flow as airflow with pressure fluctuations less than 0.06% of the mean pressure.[33] The maximum quiet pressure is the highest stagnation pressure at which there is one full second of quiet flow that contains less than 1% turbulence or turbulent bursts, and the maximum intermittently-quiet pressure has been defined as the highest stagnation pressure at which there is 0.1 seconds of quiet flow.[29] Before the past year, these two pressures were close enough in the BAM6QT that there was little reason to distinguish between them, but it became necessary when shorter-duration segments of quiet flow became seen at increasingly higher pressures.

Tests are being done in the BAM6QT to determine the size of the uniform quiet flow core and the maximum Reynolds number at which quiet flow is achieved. The maximum stagnation pressure at which quiet flow is achieved directly relates to the maximum quiet Reynolds number, though the maximum quiet pressure is not always definite and consistent.

Additional tests are being done to determine the axial uniformity of the quiet flow in the BAM6QT. Figure 17 shows RMS calculations from four quiet runs at the same initial stagnation pressure of 90 psia. The pitot tube pressure transducer was placed at four different axial locations along the tunnel centerline. z is defined as the axial distance downstream of the throat. From these comparisons it is evident that while the first two seconds of each run consistently have low noise levels, after two seconds there is an increase in noise. Here, the noise levels are still well within the definition of quiet flow, but further tests are being done to determine the cause and trends of this increase, which is currently uncertain.

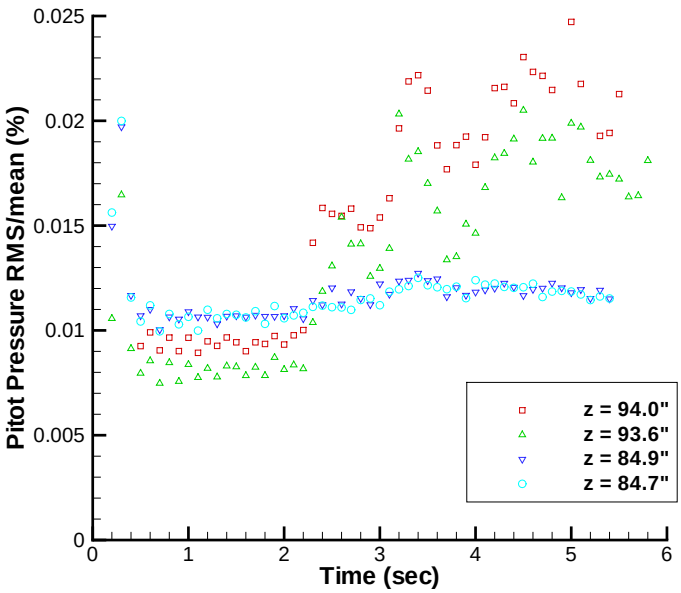

Figure 17. RMS/mean calculations from Kulite pressure transducer pitot probe at four axial locations under quiet flow along the tunnel centerline. Initial stagnation pressure was 90 psia.

IV.C. Effect of Suction Slot on Noise from Turbulent Nozzle-Wall Boundary Layer

It has been suggested that when the air is not suctioned over the bleed lip and a turbulent boundary layer is generated by the bleed lip serving as a trip, the BAM6QT may be noisier than conventional wind tunnels. To check the noise generated by the closed bleed slot, a Kulite pressure transducer pitot probe was run

twice, above the BAM6QT maximum intermittently-quiet pressure, once with the bleed slot open and once with the bleed slot closed. For these runs, the BAM6QT maximum intermittently-quiet pressure was near 160 psia. At high pressures above 200 psia, the nozzle-wall boundary layer is fully turbulent whether the suction slot is open or closed. For these tests, the RMS noise levels were calculated for 0.1-second intervals and normalized by the mean pressure. The results are shown in Figure 18(a), plotting RMS/mean against the falling stagnation pressure.

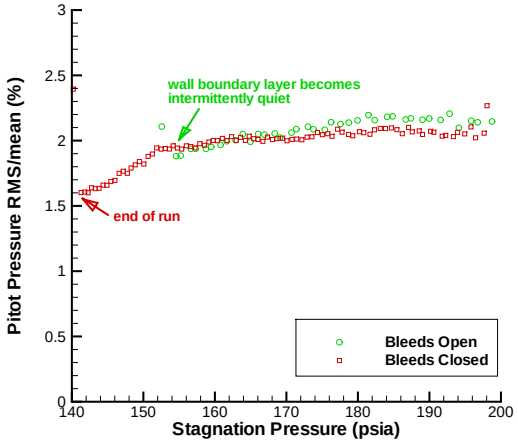

(a) RMS fluctuations

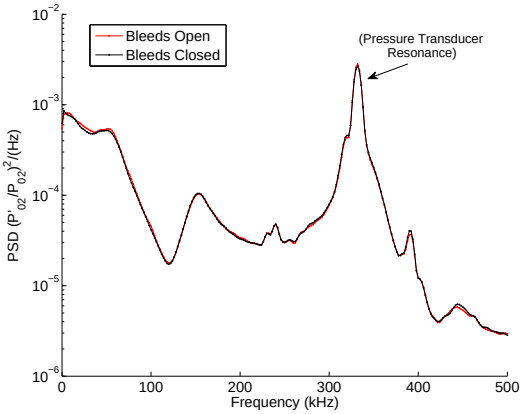

(b) Power Spectral Density of RMS fluctuations. $t = 0.4$ seconds and $P_0 = 196$ psia for both runs

Figure 18. Kulite pressure transducer probe positioned at z=84.9 in. downstream of the throat along the centerline, just upstream of the test section. The nozzle-wall boundary layer becomes intermittently quiet for the suction-slot-open run at approximately 155 psia, and the run ends for the suction-slot-closed test at approximately 140 psia.

This suggests that any air circulating around the bleed lip under noisy flow has little to no effect on the pressure fluctuations in the BAM6QT, since the noise levels are nearly the same for both cases. The noise radiated from the turbulent boundary layer near the nozzle exit is apparently unaffected by the bleed slot 7 feet upstream. A comparison of the power spectral density for these two runs is also shown in Figure 18(b). This plot shows that the power spectral densities for these two runs were nearly identical. These two spectra were taken for the same time and stagnation pressure during each run.

IV.D. RMS levels vs. Stagnation Pressure for Noisy Flow

Previous measurements in the BAM6QT have suggested that there is a correlation between the noise level and the stagnation pressure for a turbulent nozzle-wall boundary layer.[34] To explore this, the BAM6QT was run at different initial stagnation pressures with a pitot probe held at $z = 93.6$ inches downstream of the throat on the tunnel centerline with the suction slot closed. The noise levels were calculated for 0.1-second intervals and plotted versus their mean stagnation pressure, which decreases over the course of the run. The results are shown in Figure 19.

The general trend in this figure suggests that under noisy flow, as stagnation pressure increases the normalized tunnel noise decreases. This is similar to the results found by Laderman in Reference 35. However, these three runs are over a limited range of initial stagnation pressures, and additional tests are being done to determine if and how this trend continues at lower and higher pressures. It is likely that there are still effects of time-dependence in these runs.

IV.E. Recent Operational Difficulties

A new stainless-steel nozzle is being manufactured for the BAM6QT which can withstand higher temperatures. To make sure this nozzle will fit properly, test pieces have been manufactured and tested on the existing nozzle. Each round of tests has required opening the BAM6QT nozzle at the throat as well as further downstream. Historically, each time the throat is opened and reclosed there is a variation in performance.[36,37]

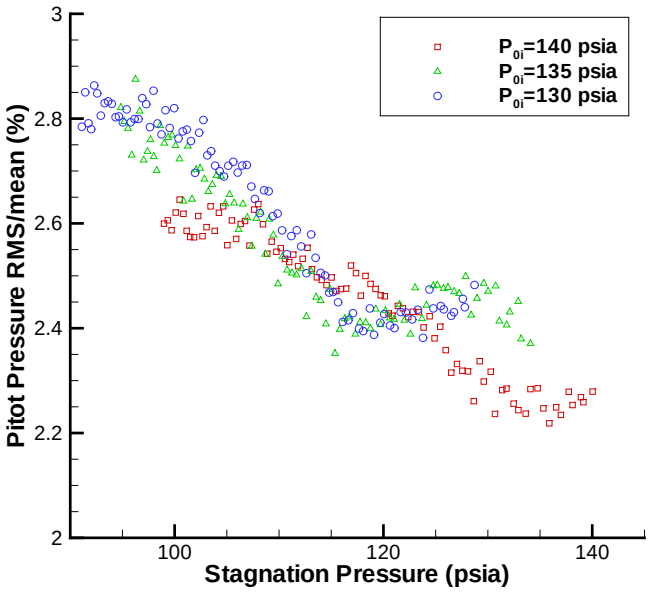

Figure 19. Pitot RMS fluctuation levels normalized by the mean for 3 runs with the suction slot closed. Each color and symbol represents a separate run. Stagnation pressure falls as time progresses.

The nozzle throat was opened in March for the first round of measurements. A few runs made before this showed a maximum quiet pressure up to 159 psia, with one turbulent burst or less for the first two seconds of run time. After the throat was opened and reclosed, the maximum intermittently-quiet pressure decreased to 89.9 psia, but after 3 more runs it increased to 123 psia, and after about another 25 high-pressure runs, it was restored to 149 psia. Additional runs showed high-pressure quiet runs with less turbulent bursts than in February, with a maximum quiet pressure of 146 psia.

The nozzle throat was again opened and reclosed in May for additional measurements. After three runs the maximum intermittently-quiet pressure was 92.2 psia, and after another 19 high-pressure runs it was still at 92 psia. Additional runs have seen little change, and it was uncertain what could have been triggering transition at this lower pressure. It was suspected that the bleed lip had not been properly cleaned before closing, and so the nozzle throat was opened once more in June.

IV.F. Summary of Results

An axial dependence of noise levels for quiet flow has been seen in the BAM6QT, though noise levels at the nozzle exit on the centerline are low enough to still be considered quiet. When the nozzle-wall boundary layer is turbulent, the conventional noise levels are not affected by whether the bleed slot is opened or closed. This suggests that with the bleeds closed the tunnel is nominally conventional. Measurements of the same probe location with different initial stagnation pressures have shown a correlation between noise levels and stagnation pressure for noisy flow.

V. Instability Measurements on a Circular-Arc Compression Cone

A 0.47-m-long, 3-m circular-arc flared cone with a 0.16-mm-radius nosetip was run in the BAM6QT to study natural transition under fully quiet flow. This cone creates a very unstable boundary layer, in which second-mode waves reach high amplification factors. The original design used a 0.45-m-long cone with 1-mm-radius blunt nose tip with an initial angle of 2°. This cone provided an N-factor of 13 at $p_0 = 140$ psia, but transition was not observed.[7] Since a sharper nosetip is expected to provide larger amplitudes,[38] a 0.16-mm-radius nosetip was made. Amplification factors of up to $N = 22$ at a stagnation pressure of $p_0 = 150$ psia

are possible for this "nearly sharp" nosetip configuration.[29]

Experiments in October on the compression cone showed streamwise streaks which weaken and grow again in quiet flow.[29] After reviewing computations by Li,[39] an experiment was designed to attempt to control the spacing of the streamwise streaks. Roughness dots were to be placed at a location on the cone where the streamwise streaks are expected to start growing, similar to the work done by Saric, et al.[40] PCB 132A31 transducers were used to measure pressure fluctuations along the surface of the cone. Temperature-sensitive paint was used to visualize the transition location and flow structures such as hot streaks from vortices.

V.A. Control of Streamwise Vorticity with Roughnesses

One of the proposed causes of the streamwise streaks is an interaction between Görtler vortices and second-mode waves. Computations were made at NASA Langley by Li[39] to determine the N-factors of the Görtler instability along the surface of the compression cone for different azimuthal spacings of vortices. These computations show that between an azimuthal spacing of $n = 50$ and $n = 100$, where n is the number of vortices around the cone, the maximum N-factor of the Görtler vortices changes only by 1 out of a maximum $N = 5$. This indicates a broad range of azimuthal spacings with similar amplification factors. Waves with an azimuthal spacing of $n = 100$ start growing at a location of about $x = 0.17$ m and waves with an azimuthal spacing of $n = 50$ start growing at a location of $x = 0.10$ m.

(a) Roughness dots spaced 4° apart ($n = 90$) upstream of paint edge.

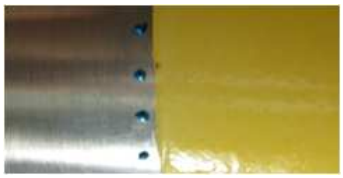

(b) Roughness dots spaced 8° apart ($n = 45$) upstream of paint edge.

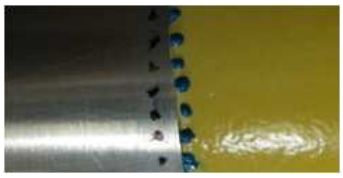

(c) Roughness dots spaced 4° apart ($n = 90$) on surface of paint. Black dots are permanent marker to indicate where dots should be placed.

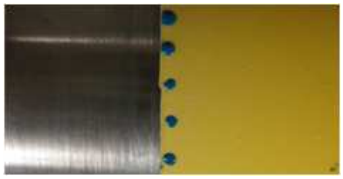

(d) Roughness dots spaced 8° apart ($n = 45$) on surface of paint.

Figure 20. Roughness dots placed upstream and on paint edge.

Roughness dots, which were approximately hemispherical in shape and 180 μm high, as measured by a dial indicator, were applied to the surface of the cone upstream of the paint edge (Figures 20(a), 20(b)) and on the edge of the painted surface (Figures 20(c), 20(d)). The roughness dots are small dots of nail polish on the surface of the compression cone. Nail polish was used to facilitate removal and addition of dots between runs. For an azimuthal spacing of $n = 100$, the Görtler waves start to grow at $x = 0.17$ m, where the circumference of the cone is only 6.3 cm. The dots were applied at a position of $x = 0.323$ m, where the circumference of the cone is 34 cm, due to a concern that the circumference of the cone may be too small to successfully apply the roughness at an azimuthal spacing of $n = 100$. This means that the Görtler waves will have grown to an amplification factor of $N = 1.9$ for azimuthal spacing $n = 100$ and to $N = 3.2$ for $n = 50$ at this location. To control the spacing of the dots, the model was mounted in an angle indexer on a mill and a permanent marker was used to mark the spacing of the dots, as shown in Figure 20(c). Due to the limitations of the angle indexer used to apply the dots, only azimuthal spacings of $n = 45$ and $n = 90$ were possible.

V.B. Instrumentation

Five PCB 132A31 fast pressure transducers were installed at $x = 0.23$ m, 0.28 m, 0.33 m, 0.38 m, and 0.43 m. These pressure transducers were used to measure second-mode wave growth along the length of the cone.

A Medtherm Schmidt-Boelter heat-transfer gage with two built-in surface and body K-type thermocouples was installed at $x = 0.45$ m. The heat transfer data will eventually aid in converting temperature-sensitive paints data to quantitative heat-transfer measurements. A Dantec 55R47 hot film was installed at $x = 0.46$ m about 15° away from the ray along which the PCBs and Schmidt-Boelter sensors were mounted. This hot-film sensor is used to provide qualitative data on whether or not the flow has transitioned at the back of the cone. The hot-film data will be presented at a later time.

Temperature-sensitive paints were also used in this experiment. Four coats of LustreKote white primer and three coats of LustreKote "Jet White" paint were used as an insulating layer. Four coats of Ru(Bpy) crystals mixed with automotive clear coat (Limco LC4000) were used as the temperature-sensitive paint. The final thickness of the paint was about 150 μm, as measured with a Elcometer 456 coating thickness gauge. Images were taken with a pco.1600 CCD camera using 2×2 binning and one analog-to-digital converter at a frame rate of 27 Hz. The registration marks in the image are spaced 30° apart azimuthally and 2.54 cm apart longitudinally. Images are processed by comparing a "flow on" image taken while the tunnel is running with a "flow off" image, which is taken while the tunnel is pressurized, but there is no flow. This provides a temperature change between when the flow is on versus when the flow is off. This image is qualitatively proportional to the surface heat flux.

V.C. Experimental Results

V.C.1. TSP Measurements and Observation of Change in Hot Streaks

The first attempt at changing the spacing of the vortices was made by placing the roughness dots upstream of the edge of the painted surface. For the case where no roughness dots are placed on the surface of the cone, a set of streamwise streaks appears at $x = 0.387$ m in Figure 21(a). The temperature of this region increases by about 8°C, when compared to an image where there is no flow.

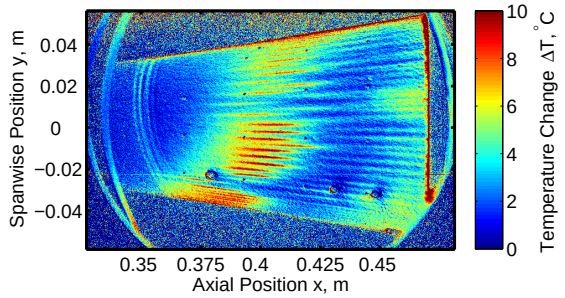

(a) No roughness dots on surface of cone. $p_0 = 140.3$ psia, $T_0 = 151.4$°C.

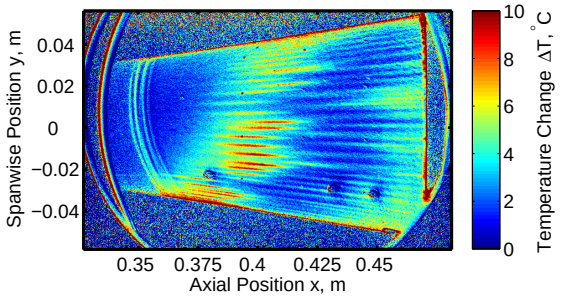

(b) Roughness dots spaced 8° apart azimuthally ($n = 45$). $p_0 = 140.0$ psia, $T_0 = 151.3$°C.

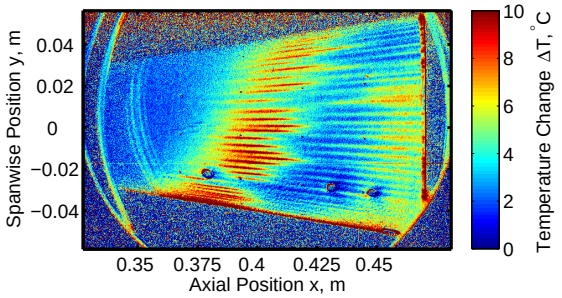

(c) Roughness dots spaced 4° apart azimuthally ($n = 90$). $p_0 = 139.2$ psia, $T_0 = 152.9$°C.

Figure 21. Temperature-sensitive paints images with roughness dots placed upstream of the paint edge. Two PCB 132A31 sensors are visible at $x = 0.38$ m and $x = 0.43$ m. A Schmidt-Boelter gage is visible at $x = 0.45$ m. Flow is from left to right.

For the results shown in Figure 21(b), roughness dots were placed upstream of the temperature-sensitive paint 8° apart, at an azimuthal spacing of $n = 45$, at a location of $x = 0.321$ m. Some slight changes in the streak spacing are seen, particularly between $x = 0.382$ m and $x = 0.415$ m and $y = 0.0$ m and $y =$ -0.02 m.

It is unclear, however, whether or not the spacing of these vortices has matched the spacing of the roughness dots. Figure 21(c) shows the results from placing roughness dots upstream of the paint spaced 4° apart, at an azimuthal spacing of $n = 90$. There is again a definite change in the spacing of the streamwise streaks. However, once again it is unclear whether the spacing has been changed to the same spacing as the roughness dots. It is possible that the generation of the streamwise streaks is dominated by the step at the beginning of the paint, rather than by the dots. To eliminate this step, a new cone may have to be constructed, where the upstream portion of the frustum is 200 μm larger in radius than the downstream portion, assuming the same paint thickness.

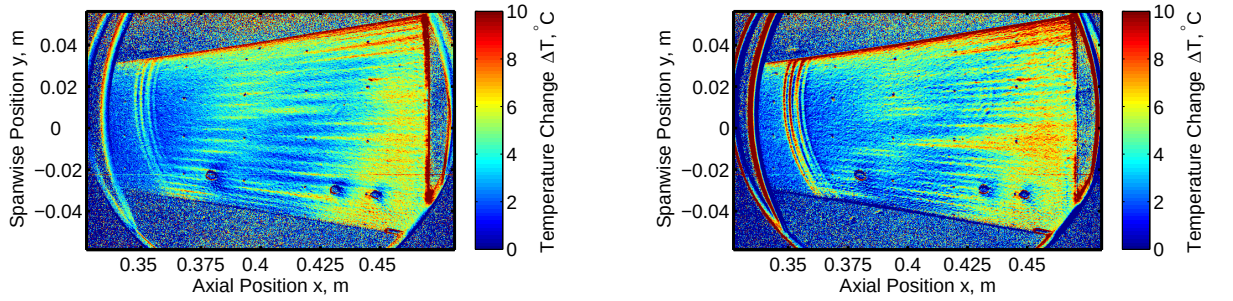

(a) Roughness dots spaced 8° apart azimuthally ($n = 45$). $p_0 = 141.8$ psia, $T_0 = 150.1°$C

(b) Roughness dots spaced 4° apart azimuthally ($n = 90$). $p_0 = 138.8$ psia, $T_0 = 155.1°$C

Figure 22. Temperature-sensitive paints images showing a difference in streak spacing based upon the change in spacing of roughness dots when dots are placed on top of the paint. Two PCB 132A31 sensors are visible at $x = 0.38$ m and $x = 0.43$ m. A Schmidt-Boelter gage is visible at $x = 0.45$ m. Flow is from left to right.

Dots were then placed on top of the paint edge in order to eliminate the effects of having a forward-facing step behind the roughness dots (Figures 20(c), 20(d)). This created a roughness almost twice the height of the paint thickness when the dot height was added to the span-uniform paint. The final height of the dots on top of the paint was 300 μm, and almost 30% of the boundary layer thickness, which is roughly 1 mm at 140 psia. Figure 22(a) shows the results of placing roughness dots 8° apart on the edge of the paint surface at $x = 0.324$ m. At an axial location between $x = 0.382$ m and $x = 0.415$ m and spanwise location between $y =$ -0.02 m and $y = 0.02$ m, roughly 60° of the cone is visible. Between the two outermost rays of registration marks visible in this zone, about seven streamwise streaks are seen, indicating that the spacing of these streaks is about 8°. This shows that the spacing of the streaks has been changed to match the spacing of the roughness dots. Figure 22(b) shows the results of placing roughness dots 4° apart. The number of vortices between $y = \pm 0.02$ m in Figure 22(b) is twice what is seen in the same region in Figure 22(a) at about 15 streaks. The spacing of the streaks in these images is again the same as the spacing of the roughness dots.

Thus the spacing of dots can change the spacing of the streamwise streaks. This indicates that the streamwise vortices can be controlled, and that the secondary instability on the surface of the cone may have a significant effect. Further tests will have to be done with dots farther upstream, where the Görtler vortices start growing with dots that are more controlled in size and shape.

V.C.2. Comparison of Temperature-Sensitive Paint Images and Sensor Data

On a typical 7° half-angle cone at 0° angle of attack at Mach 6, transition is caused by the growth of second-mode waves. As measurements are taken farther downstream (comparing the red trace to the blue trace in Figure 23(a)), the amplitude of the pressure fluctuations increases. The peak frequency of the second-mode waves on a straight 7° half-angle cone will decrease because the boundary layer increases along the length of the cone and the second-mode frequency is related to the boundary-layer thickness. This shift in frequency is not seen on the compression cone, as it was designed to have a constant boundary-layer thickness. Turbulence, as seen by PCB 132A31 pressure sensors, is characterized by a broad band of frequencies with no distinct peak (green trace in Figure 23(a)).

When no roughness dots are present on the surface of the compression cone, the PCB 132A31 power spectra appear as in Figure 23(b). As measurements are made farther downstream, the peak at 298 kHz increases in amplitude until $x = 0.38$ m. Downstream to $x = 0.43$ m, perhaps due to the onset of transition, the amplitude of the wave decreases. Also of note are the peaks that appear at 583 kHz and 893 kHz in the

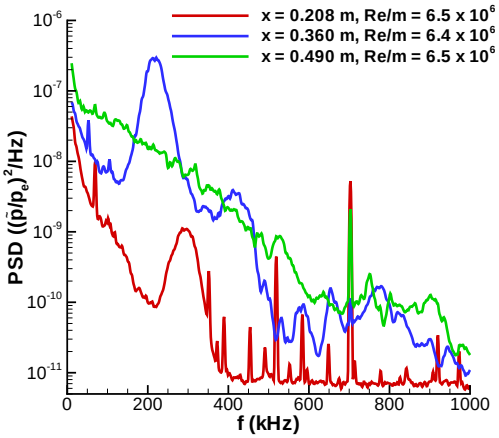

(a) Example PCB 132A31 data from a 7° half-angle cone from Reference 34.

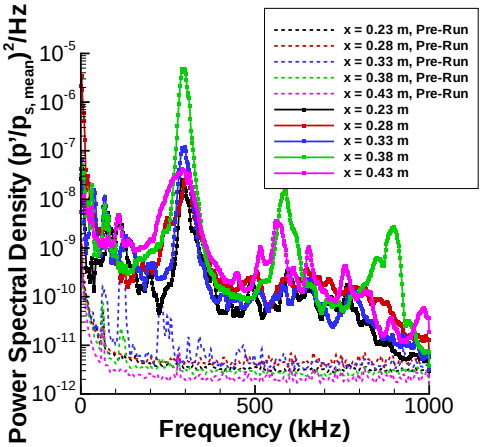

(b) Compression cone with no dots. $p_0 = 140.3$ psia, $T_0 = 151.4°$C. (Same run as Figure 21(a).)

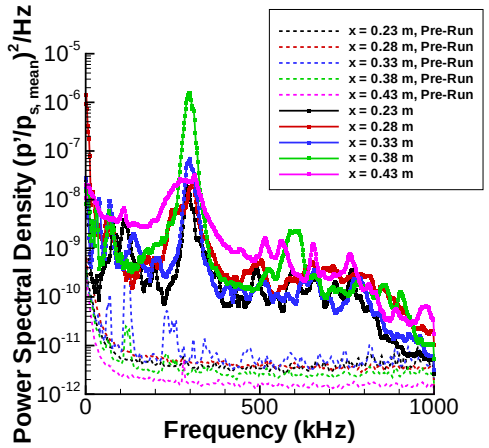

(c) Compression cone with roughness dots spaced 8° apart ($n = 45$). $p_0 = 141.8$ psia, $T_0 = 150.1°$C. (Same run as Figure 22(a).)

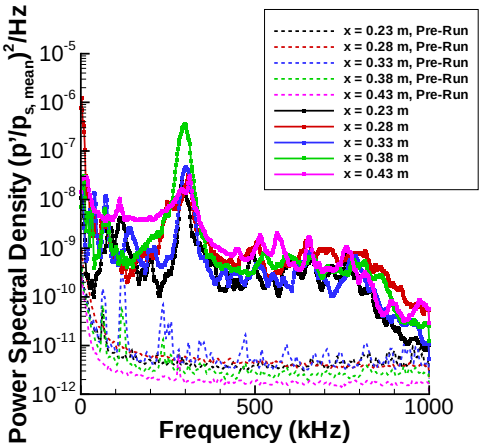

(d) Compression cone with roughness dots spaced 4° apart ($n = 90$). $p_0 = 138.8$ psia, $T_0 = 155.1°$C. (Same run as Figure 22(b).)

Figure 23. Power spectra of pressure fluctuations measured by PCB 132A31 sensors for cases with roughness dots on top of paint surface.

$x = 0.38$ m (green trace in Figure 23(b)). These are likely harmonics of the second-mode wave peak. In the TSP images, the streamwise streaks appear on the surface of the compression cone at about the location where the harmonics appear. These harmonics are not as prominent at a location of $x = 0.43$ m (magenta trace in Figure 23(b)), but at this location, the streamwise streaks have begun to weaken.

Power spectra for when roughness dots are placed on top of the paint at a separation of 4° apart (Figure 23(c)) and a separation of 8° apart (Figure 23(d)) show similar trends. Growth in the second-mode wave peak is seen up until a location of $x = 0.38$ m. For the case of $n = 45$, at $x = 0.43$ m, the second-mode wave peak is broader than at $x = 0.38$ m and the amplitude is lower. There is also a slight increase in the amplitude of other frequencies, but not enough to engulf the second-mode wave peak. For $n = 90$, the peak in the trace for $x = 0.43$ m is broader and shaped differently from the upstream peaks, but the background noise at frequencies greater than 300 kHz does not seem to rise. A possible second harmonic of the second-mode wave peak is seen for a spacing of $n = 45$ (Figure 23(c)) at $x = 0.38$ m, but not for a spacing of $n = 90$ (Figure 23(d)). In the temperature-sensitive paints images (Figure 22), the streamwise streaks start to spread at around $x = 0.45$ m. It is not clear why the higher harmonics are not present when the roughness dots are applied. The increase in broadband fluctuations between 0 kHz and 300 kHz at $x = 0.43$ m may indicate the onset of transition.

V.C.3. N-Factor at Transition Onset

Streamwise cuts of the temperature change along the compression cone were taken to compare with the computations of wall heat flux. An indirect comparison can be made because the wall heat flux is proportional to the temperature change, therefore the experiment should show the same qualitative trends as the computations. Streamwise temperature profiles were taken along rays on the cone's surface, at the 15 locations marked by as heavy black lines in Figure 24. These temperature profiles were then averaged for each of the runs as shown in Figure 25 to get an idea of average temperature change as a function of axial location. Some stray artifacts present in the temperature-sensitive paints images appear in these streamwise temperature profiles. At $x = 0.35$ m, for example, a reflection from the window is shown as a small peak in temperature in Figure 25. Stray points, such as seen at $x = 0.38$ m in the green trace on Figure 25, are from sensors or registration marks.

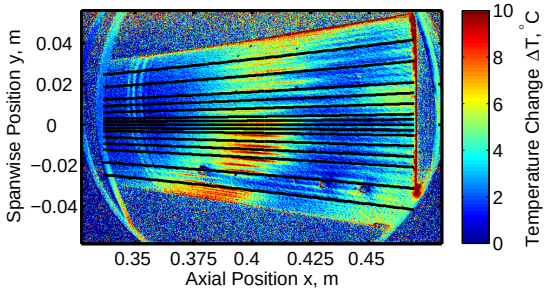

Figure 24. Locations of streamwise cuts of temperature change along the compression cone shown on a typical temperature-sensitive paints image.

When no roughness dots were present (red '+' in Figure 25), the temperature change increases from $x = 0.36$ m until $x = 0.395$ m. This increase in heating is likely due to the streamwise vortices. Then, the temperature change decreases until $x = 0.44$ m. At $x = 0.44$ m, the heating begins to increase again. It is unclear whether or not the flow transitions at the back of the cone, as the cone is not long enough to show if the heating remains constant after this area of reheating.

When roughness dots were placed upstream of the paints (blue diamonds and green triangles in Figure 25), the temperature change profile follows roughly the same trends as the case where there are no roughness dots. It is likely that the trends are very similar due to the fact that the dot heights are close to the height of the paint edge. Again, it is unclear whether or not the flow transitions here due to the short length of the cone.

For the cases where the roughness dots were placed on top of the paint (cyan circles and magenta squares in Figure 25), the temperature change profile looks more similar to a transitional profile. The heating remains fairly constant along the cone until $x = 0.42$ m for both the $n = 45$ and $n = 90$ cases. After this, the heating increases until about $x = 0.45$ m, where the heating appears to be leveling out again.

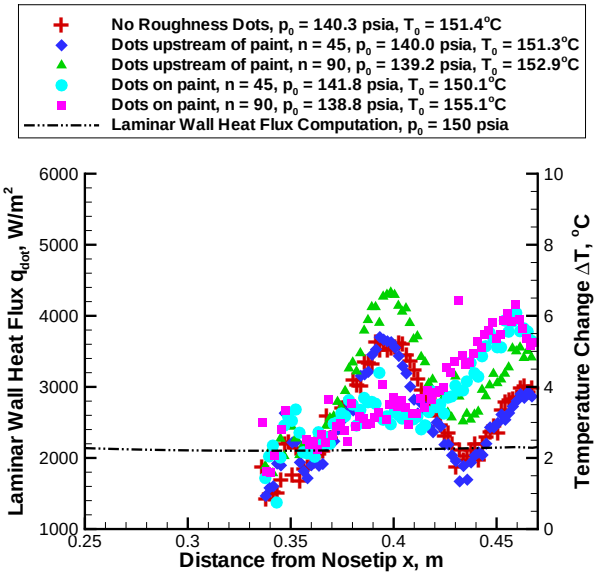

Figure 25. Temperature change profile from an average of 15 streamwise cuts along the compression cone.

Figure 26 shows the computed N-factor for the compression cone at $p_0 = 150$ psia with locations of interested highlighted. The first arrow at $x = 0.38$ m is the location where the streamwise streaks first appear on all cases, according to Figure 25. The N-factor at this location is $N = 15.0$. In the cases where no roughness dots were used or the dots were placed upstream of the paint edge, the streamwise streaks start to reheat at a location of $x = 0.438$ m. The N-factor at this location is $N = 20.0$. For the case where dots are placed on top of the paint, the streamwise streaks start heating at $x = 0.415$ m, where the N-factor is 18.4. If the start of increase in heating is taken to be the transition onset location for the case with dots on top of the paint, the N-factor at transition can be taken as $N = 18.4$.

V.D. Summary of Results

Roughness dots placed upstream of the edge of the temperature-sensitive paint seem to have little effect on altering the spacing of streamwise streaks and the heating on the surface of the compression cone. It is likely that in this case, the paint edge still dominates the generation of streamwise vorticity. When roughness dots are placed on top of the paint, the spacing of the streamwise streaks seen in the temperature-sensitive paints can be changed. A combination of the temperature-sensitive paints data and PCB sensor data for this case also indicates that the flow transitions at around $N = 18.4$.

V.E. Further Work

These measurements are only a beginning that suggests an apparently fruitful means of studying nonlinear breakdown under fully quiet flow. A more controlled method of applying dots of a uniform shape and size needs to be developed for this purpose. Roughness dots should also be placed farther upstream at a location between $x = 0.1$ m and $x = 0.17$ m. A new compression cone with a backward-facing step could also be constructed to eliminate the effects of the forward-facing step created by adding a temperature-sensitive paint layer.

VI. Crossflow Instability and Transition on a Cone at Angle of Attack

An axisymmetric cone in hypersonic flow pitched at an angle of attack creates a circumferential pressure gradient due to the shock lying closer to the body on the windward side than the leeward side. This pressure gradient causes the inviscid streamlines to be curved. In the boundary layer, the streamwise velocity is reduced, but the pressure gradient does not change, causing a secondary flow (crossflow) that is perpendicular to the inviscid streamlines. The crossflow velocity profile is inflected, which is a source of instability. This

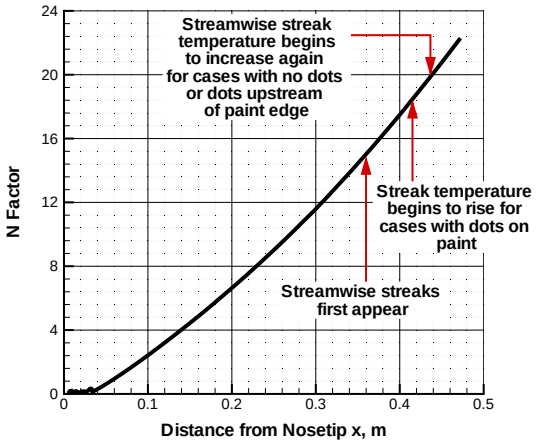

Figure 26. Computed N-factor for the compression cone at $p_0 = 150$ psia, $T_0 = 160°$. Computations from Gronvall.[29]

crossflow instability is likely to be critical on many hypersonic vehicles, yet is poorly understood.

Experiments were performed on a 7° half angle cone at 6° angle of attack in the BAM6QT to measure the effect of tunnel noise and distributed surface roughness on the crossflow instability. A new cone was designed for these studies, as shown in Figure 27. The cone is 16 inches long with a 4-inch base diameter. It includes a 6-inch long nominally sharp nosetip and 10-inch long frustum. There are six ports for sensors on the surface of the frustum, and two holes drilled in the base of the cone for coaxial thermocouples. These data will be presented at a later time. The frustum is painted with the temperature-sensitive paint, which in previous tests with an older model created a forward-facing step.[29] The radius of the frustum on the new cone was reduced by 200 μm in order to reduce this forward-facing step as much as possible. Two nosetips were fabricated. One was left with the machine finished surface, the other was polished to a mirror finish. Computations by Choudhari[41] have shown that the neutral point of the most amplified stationary waves occur at an axial distance of roughly 2-3 inches from nosetip. While previous results have shown the effect of varying the average surface roughness over the frustum,[29] this paper examines the effect of varying the distributed roughness close to the neutral point of the most amplified stationary waves.

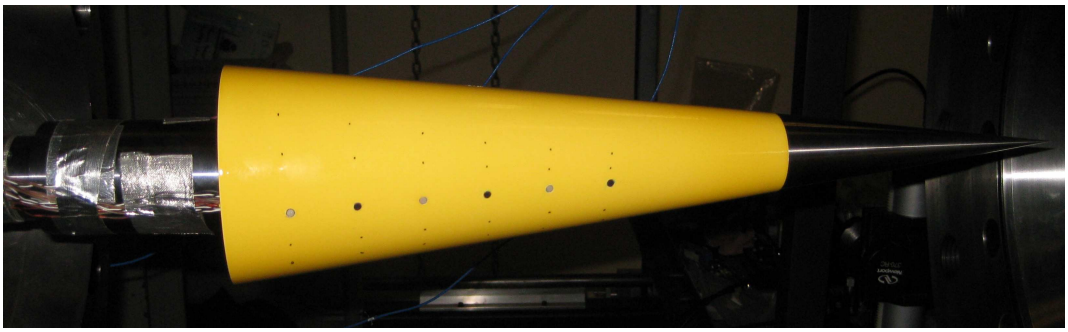

Figure 27. 7° half angle cone at 6° angle of attack installed in the BAM6QT with the machine finished nosetip.

VI.A. Instrumentation

As described earlier, temperature-sensitive paint is used to obtain a global temperature distribution and was only applied to the frustum. The painting procedure and data acquisition setup was the same as described in section V.B, except two analog to digital converters were used allowing the pco.1600 CCD camera to capture images at 53 frames per second.

VI.B. Surface Characteristics

The average roughness of the paint, machine finished nosetip and polished nosetip were determined by a Mitutoyo Surftest SJ-301 profilometer. The average roughness is defined as the mean of the absolute values of the deviations from the mean height. The profilometer was traversed over a 4.0 mm length at 3 random locations and the results were averaged. These values are shown in Table 3. The painted surface and the machine finish nosetip have a similar average roughness. The polished nosetip has an average roughness an order of magnitude less.

Table 3. Summary of the average roughness for the painted surface, polished nosetip and machine finished nosetip.

	Average roughness [μm]
Painted Surface	0.33
Machine Finished Nosetip	0.38
Polished Nosetip	0.04

As mentioned before, the radius of the frustum was reduced by 200 μm to account for the thickness of the paint. The step in the paint was measured with the profilometer for both nosetips, traversing it over a 2 mm length. Measurements were taken at 5 random locations for each nosetip. Table 4 shows the range of steps found. It was decided not to average the results because such a large range was found. The upper end of the step range is similar to the forward-facing step found in the author's previous work.[29] It is also noteworthy that the step for the polished nosetip on average is larger than the machine finished nosetip. This is due to the removal of some material during the polishing process. Thus, the first paint job with the new cone design was not yet successful in matching the backward facing step of the frustum and creating a smooth surface. It was decided to run the cone anyways with the forward-facing step to see if altering the nosetip roughness would still have an effect. In future experiments, either the frustum radius or the paint thickness will be reduced to minimize the step at the nosetip-frustum junction.

Table 4. Summary of the foward-facing step at the nosetip-frustum junction due to the TSP with both nosetips.

	Forward-facing step height [μm]
Machine Finished Nosetip	41 - 76
Polished Nosetip	43 - 82

VI.C. Effect of Varying Distributed Roughness and Tunnel Noise

Measurements were taken for the polished (Figure 28(a)) and machine-finished nosetips (Figure 28(b)) at a freestream unit Reynolds number of 6.3×10^6 m^{-1} under quiet flow. Flow is from left to right. ΔT refers to the number of degrees Celsius above the pre-run temperature. There is only one clear stationary vortex forming with the polished nosetip, originating at roughly x = 0.31 m and y = 0.1 m. although others are faintly visible. There are two clearly distinguishable stationary vortices formed with the machine finished nosetip, originating at roughly x = 0.35 m, y = 0.05 m and x = 0.31 m and y = 0.1 m. The latter stationary vortex appears to form with both nosetips. Disregard the vertical line that appears at roughly an axial location of 0.34 m. This is an artifact of using two analog to digital converters that appears during the realignment of the flow on and flow off images. Unfortunately this was the maximum attainable quiet unit Reynolds number at the time, as explained in section IV.E.

Figure 29 shows the surface temperature plotted with the spanwise distance at an axial distance of 0.37 m. Three pixels in the axial distance were averaged, where one pixel is roughly 0.021 mm. The two vortices created with the machine finished nosetip are clear in this plot, showing up as the two peaks. The one perceived vortex with the polished nosetip is not as clear. Not only are there two vortices forming with the machine finished nosetip, these vortices exhibit a higher amplitude. It is also noteworthy that the overall temperature increase of the surface with the machine-finished nosetip is roughly 0.5°C higher. It is not clear from this data how much of an effect the forward-facing step at the nose-frustum junction has as compared

to the average surface roughness of the nosetips. It is also not clear if the higher surface temperature with the machine-finished nosetip is a repeatable phenomena.

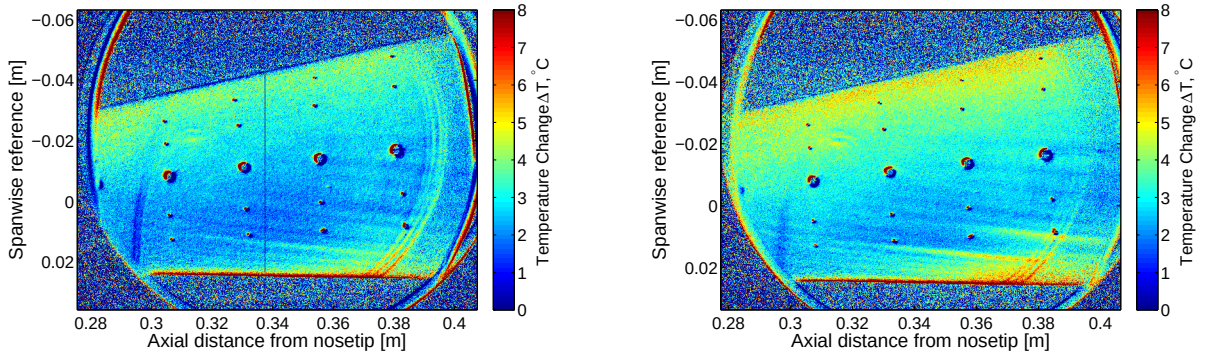

(a) Polished nosetip. $p_0 = 95$ psia, $T_0 = 158.2°$C

(b) Machine finished nosetip. $p_0 = 95$ psia, $T_0 = 156.8°$C

Figure 28. Temperature-sensitive paints images showing the effect of changing the distributed roughness on the nosetip under quiet flow for a unit Reynolds number of 6.3×10^6 m^{-1}. Side view of the cone

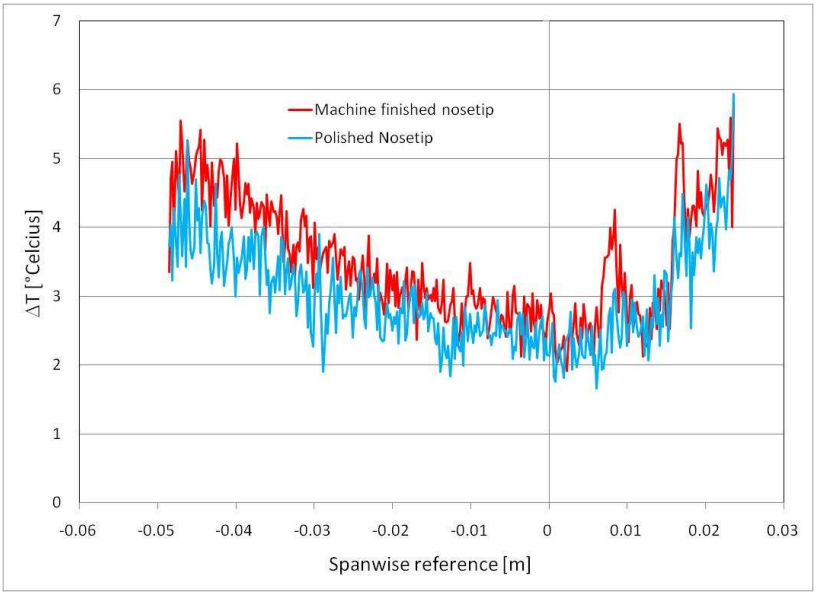

Figure 29. Spanwise temperature profiles at an axial distance of 0.37 m for both the of the images shown in Figure 28.

Experiments done at a unit Reynolds number 6.3×10^6 m^{-1} under noisy flow are shown in Figure 30. This is the same unit Reynolds number as shown in Figure 28 (under quiet flow). Unlike the previous results,[29] there is not an obvious effect of tunnel noise on the crossflow instability, although these previous results were performed at a higher quiet Reynolds number. The stationary vortices are visible farther upstream under quiet flow. Stationary vortices may dominate in low-noise environments, which would explain why they are visible farther upstream on the cone. There is also not an obvious effect of the nosetip surface roughness under noisy flow. The stationary vortices become visible at roughly the same axial location, and appear to reach the same amplitude. This suggests that the forward-facing step has a more significant effect than the nosetip roughness.

Figure 31 shows spanwise temperature profiles for a unit Reynolds number of 6.3×10^6 m^{-1} with both nosetips under noisy and quiet flow. These profiles were taken at an axial distance of 0.37 m. The only temperature profile that shows a significant difference is the machine finished nosetip under quiet flow. Once again, in this profile the two stationary vortices are easily visible. The cases with the machine finished nosetip do tend to show a higher temperature near the windward ray, but it is not clear why this is the case. Once again it is difficult to separate the effect of the forward-facing step in the paint and the surface roughness of the nosetip.

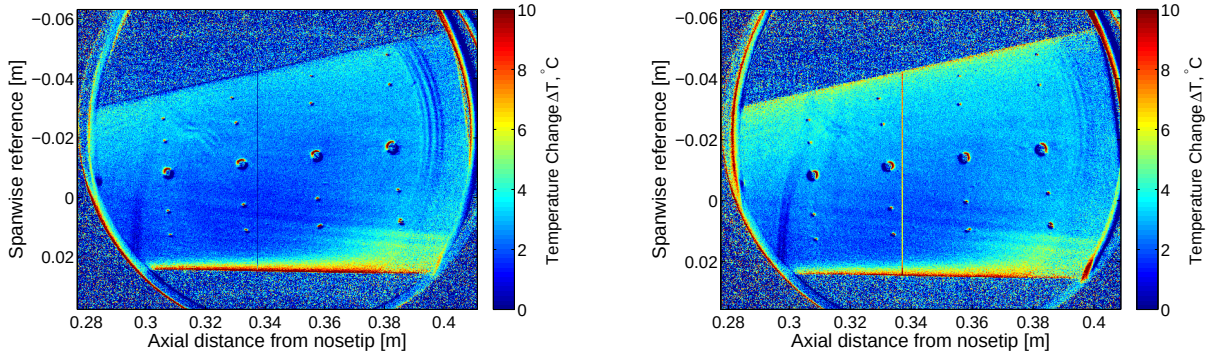

(a) Polished nosetip. $p_0 = 88$ psia, $T_0 = 156.0°$C

(b) Machine finished nosetip. $p_0 = 88$ psia, $T_0 = 158.0°$C

Figure 30. Temperature-sensitive paints images showing the effect of changing the distributed roughness on the nosetip under noisy flow for a unit Reynolds number of 6.3×10^6 m^{-1}. Side view of the cone.

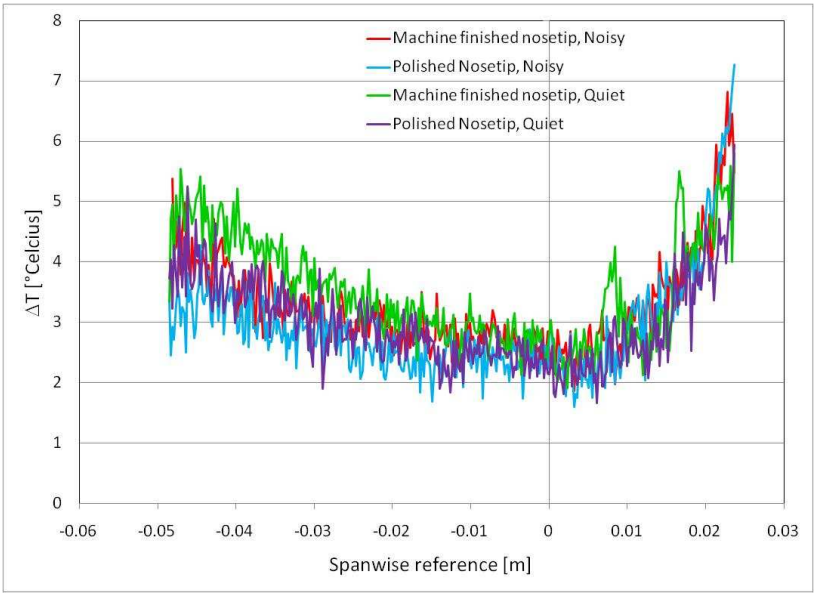

Figure 31. Spanwise temperature profiles at an axial distance of 0.37 m for the images shown in Figures 30 and 28.

The next set of tests were done at a higher unit Reynolds number of 9.0×10^6 m^{-1} with both nosetips. These results are shown in Figure 32. There is no discernible difference between the two cases. For both cases there are two distinct stationary vortices near the leeward ray that appear to break down originating at roughly the same axial location. The transition front (inferred by the increase in surface temperature) can be seen moving towards the windward ray from the side. Once again this is most likely because the forward-facing step is dominating the generation of the stationary vortices. It is also possible that the axial location of the neutral point of the most amplified traveling waves is not the same as the stationary waves, therefore altering the roughness near the latter neutral point will not have a noticeable effect under noisy flow (where traveling waves may dominate).

Plotted in Figure 33 are spanwise temperature profiles at an axial distance of x = 0.35 m for the TSP images in Figure 32. Once again 3 pixels were averaged in the axial direction. For both nosetips, a similar trend is shown. An increase in temperature is seen as the transition front is traversed at approximately y = -0.035 m. The onset of transition is inferred to be where an increase in surface temperature is seen. The rise in temperature at y = 0.01 m is caused by the stationary vortex. The magnitude of this vortex is roughly the same for both cases. The temperature then tends to increase going farther towards the leeward ray, suggesting that the boundary layer is transitional or turbulent. The average change in temperature is slightly larger for the polished nosetip, but it is not clear why this is the case and if it is repeatable.

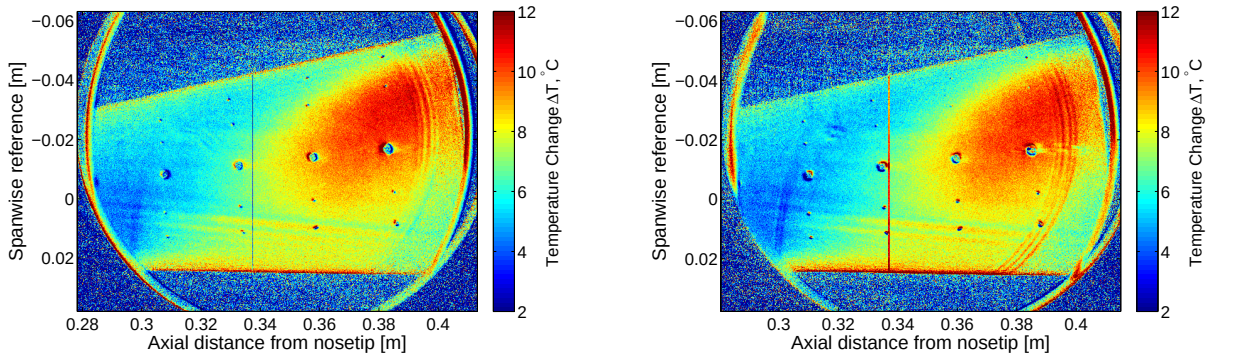

(a) Polished nosetip. $p_0 = 120$ psia, $T_0 = 155.9°$C

(b) Machine finished nosetip. $p_0 = 120$ psia, $T_0 = 156.0°$C

Figure 32. Temperature-sensitive paints images showing the effect of changing the distributed roughness on the nosetip under noisy flow for a unit Reynolds number of 9.0×10^6 m^{-1} under noisy flow. Side view of the cone.

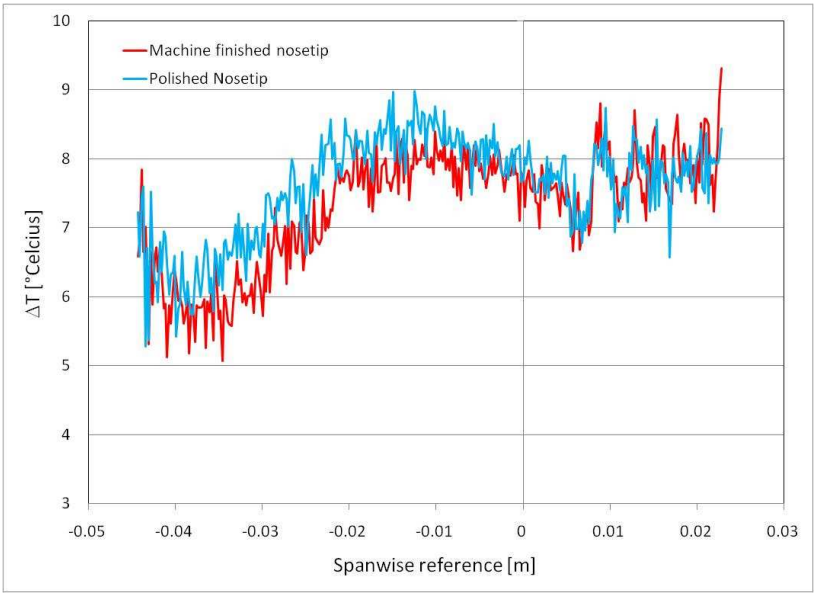

Figure 33. Spanwise temperature profiles at an axial distance of 0.35 m for both the of the images shown in Figure 32.

VI.D. Future Work

It was at first surprising that a polished nosetip with an average roughness 10 times less than a machine finished nosetip would not create a substantial difference in the amplitudes of the stationary instability. Upon further review, it appears that the forward-facing step size at the beginning of the temperature-sensitive paint is dominating the vortex generation. Until this step size is reduced sufficiently, it will not be possible to separate the effect of the step and the effect of the nosetip surface roughness. This will be done in future experiments by either reducing the radius of the frustum, or reducing the paint thickness. It is also necessary to run the cone at higher quiet Reynolds numbers when possible. The increased amplitudes of the stationary waves under higher quiet Reynolds numbers may allow the change in nosetip roughness to show a greater effect.

VII. Conclusion

Measurements were made within the wake of a 10.2-mm high cylindrical roughness in the laminar boundary-layer of the BAM6QT nozzle wall. PCB and Kulite sensors were flush-mounted in the wall. These non-intrusive measurements have verified the instability near 21 kHz previously reported in References 7–9. The 21 kHz instability is believed to be first of its kind to be detected at hypersonic speeds.

A second instability was detected and occurs at higher frequencies of 40–60 kHz. Its frequency appears to vary greatly with freestream Reynolds number. The second instability occurs at Re_k near 20,000–30,000 and a height ratio of $k/\delta \approx 0.9$–1.0. This instability breaks down farther from the roughness (greater than 60 diameters downstream) and would require additional instrumentation farther from the roughness.

A 3-m circular arc compression cone was run with a nearly sharp nosetip (initial radius of 0.16 mm). Temperature-sensitive paint was used to obtain a global temperature distribution. Roughness dots placed upstream of the edge of the temperature-sensitive paint seem to have little effect on altering the spacing of streamwise streaks and the heating on the surface of the compression cone. These streamwise streaks are likely to be caused by the interaction of Görtler vortices and second mode waves. It is probable that in the case with the dots upstream of the paint, the paint edge still dominates the generation of streamwise vorticity. When roughness dots are placed on top of the paint, the spacing of the streamwise streaks seen in the temperature-sensitive paints can be changed to match the azimuthal spacing of the dots. A combination of the temperature-sensitive paints data and PCB sensor data for this case also indicates that the flow transitions near $N = 18$.

In an effort to investigate the effect surface roughness near the nosetip on the crossflow instability, a 7° half-angle cone was tested at 6° angle of attack with temperature-sensitive paint. Two nosetips were used, with one polished to a mirror finish. The average distributed surface roughness was roughly an order of magnitude less on the polished nosestip. However, the smaller nosetip roughness had no apparent effect. It appears that the remaining forward-facing step at the leading edge of the paint may dominate.

Heat-transfer measurements were made at the stagnation point of two hemisphere models in an effort to characterize the effect of tunnel noise on heating rates. The hemispheres were equipped with coaxial thermocouples and Schmidt-Boelter heat transfer gages respectively near the stagnation point. No effect was found on these two models within the accuracy and resolution of the present measurements.

The current maximum quiet stagnation pressure of the BAM6QT is less than 92 psia, which is substantially lower than the maximum quiet stagnation pressure observed until March 2010. The decrease was apparently caused when the throat was opened, and may be due to dust or roughness. An axial dependence of centerline noise levels under quiet flow has been seen in the BAM6QT, although noise levels are still low enough to be considered quiet. Finally, when the bleed slot was closed, the BAM6QT was shown to run with nominally conventional noise levels.

Acknowledgments

This research is funded by AFOSR under grants FA9550-09-1-0191 and FA9550-08-1-0290, by an NDSEG Fellowship, and by the NASA CUIP and NASA Fundamentals programs. Dr. Meelan Choudhari of NASA Langley provided the stability computations on the 7-deg half angle cone.

References

[1]Schneider, S. P., "Hypersonic Laminar-Turbulent Transition on Circular Cones and Scramjet Forebodies," *Progress in Aerospace Sciences*, Vol. 40, No. 1-2, 2004, pp. 1–50.

[2]Beckwith, I. and III, C. M., "Aerothermodynamics and Transition in High-Speed Wind Tunnels at NASA Langley," *Annual Review of Fluid Mechanics*, Vol. 22, 1990, pp. 419–439.

[3]Schneider, S. P., "Effects of High-Speed Tunnel Noise on Laminar-Turbulent Transition," *Journal of Spacecraft and Rockets*, Vol. 38, No. 3, May-June 2001, pp. 323–333.

[4]Schneider, S. P., "Flight Data for Boundary-Layer Transition at Hypersonic and Supersonic Speeds," *Journal of Spacecraft and Rockets*, Vol. 36, No. 1, 1999, pp. 8–20.

[5]Schneider, S. P., "Effects of Roughness on Hypersonic Boundary-Layer Transition," *Journal of Spacecraft and Rockets*, Vol. 45, No. 2, March-April 2008, pp. 193–209.

[6]Klebanoff, P. S. and Tidstrom, K. D., "Mechanism by Which a Two-Dimensional Roughness Element Induces Boundary-Layer Transition," *The Physics of Fluids*, Vol. 15, No. 7, July 1972, pp. 1173–1188.

[7]Wheaton, B. M., Juliano, T. J., Berridge, D. C., Chou, A., Gilbert, P. L., Casper, K. M., Steen, L. E., Schneider, S. P., and Johnson, H. B., "Instability and Transition Measurements in the Mach-6 Quiet Tunnel," AIAA Paper 2010-3559, June 2009.

[8]Wheaton, B. M., *Roughness-Induced Instability in a Laminar Boundary Layer at Mach 6*, Master's Thesis, Purdue University School of Aeronautics & Astronautics, West Lafayette, IN, December 2009.

[9]Wheaton, B. M. and Schneider, S. P., "Roughness-Induced Instability in a Laminar Boundary Layer at Mach 6," AIAA Paper 2010-1574, January 2010.

[10]Beresh, S. J., Henfling, J. F., Spillers, R. W., and Pruett, B. O. M., "Measurement of Fluctuating Wall Pressures Beneath a Supersonic Turbulent Boundary Layer," AIAA Paper 2010-0305, January 2010.

[11]Bartkowicz, M. D., Subbareddy, P., and Candler, G., "Simulation of Instability Growth in the Purdue Mach 6 Quiet Tunnel ," AIAA Paper 2010-4723, June 2010.

[12]Harris, J. E. and Blanchard, D. K., "Computer Program for Solving Laminar, Transitional, or Turbulent Compressible Boundary-Layer Equations for Two-Dimensional and Axisymmetric Flow," NASA Technical Report TM-83207, February 1982.

[13]Hollis, B. R., Horvath, T. J., Berger, K. T., et al., "Experimental Investigation of Project Orion Crew Exploration Vehicle Aeroheating in AEDC Tunnel 9," Tech. Rep. NASA/TP-2008-215547, NASA Langley Research Center, December 2008.

[14]Hollis, B. R., Liechty, D. S., and Wright, M. J., "Transition Onset and Turbulent Heating Measurements for the Mars Science Laboratory Entry Vehicle," AIAA Paper 2005-1437, January 2005.

[15]Faye-Petersen, R., Sarver, D., and Carroll, H., "Heat Transfer and Pressure Distributions at M = 8 on 0.028 Scale Models of the Viking Entry Vehicle," Tech. Rep. NASA CR 132413, July 1972.

[16]Boyd, C. and Howell, A., "Numerical Investigation of One-Dimensional Heat Flux Calculations," Tech. Rep. NSWCDD/TR-94/114, Naval Surface Warfare Center, October 1994.

[17]Coblish, J. J., Coulter, S. M., and Norris, J. D., "Aerothermal Measurement Improvements using Coaxial Thermocouples at AEDC Hypervelocity Wind Tunnel No. 9," AIAA Paper 2007-1467, January 2007.

[18]Touloukian, Y., *Thermophysical Properties of High Temperature Solid Materials, Volume 3: Ferrous Alloys*, Macmillian, New York, 1967.

[19]"Metallic Materials and Elements for Aerospace Vehicle Structures," Tech. Rep. MIL-HDBK-5C, 1979.

[20]Gilbert, P. L., *Effect of Tunnel Noise on Laminar Stagnation-Point Heating at Mach 6*, Master's Thesis, Purdue University School of Aeronautics & Astronautics, West Lafayette, IN, August 2010.

[21]Coblish, J. J., Private communication, February 2010.

[22]Anderson, J. D., *Hypersonic and High-Temperature Gas Dynamics*, American Institute of Aeronautics and Astronautics, Inc., Virginia, 2nd ed., 2006.

[23]Hollis, B. R., "Experimental Investigation of Project Orion Crew Exploration Vehicle Aeroheating: LaRC 20-Inch Mach 6 Air Tunnel Test 6931," Tech. Rep. NASA/TM-2009-215718, NASA Langley Research Center, April 2009.

[24]Kammeyer, M. E., "Wind Tunnel Facility Calibrations and Experimental Uncertainty," AIAA Paper 1998-2715, June 1998.

[25]Kidd, C. T. and Adams, J. C., "Fast-Response Heat-Flux Sensor for Measurement Commonality in Hypersonic Wind Tunnels," *Journal of Spacecraft and Rockets*, Vol. 38, No. 5, September 2001, pp. 719–729.

[26]Hayes, W. D. and Probstein, R. F., *Hypersonic Flow Theory*, Academic Press, 1st ed., 1959.

[27]Bertin, J. J., *Hypersonic Aerothermodynamics*, AIAA Education Series, AIAA, Washington, DC, 1st ed., 1994.

[28]Lemmon, E. and Jacobsen, R., "Viscosity and Thermal Conductivity for Nitrogen, Oxygen, Argon, and Air," *International Journal of Thermophysics*, Vol. 25, No. 1, January 2004, pp. 21–69.

[29]Berridge, D. C., Chou, A., Ward, C. A., Steen, L. E., Gilbert, P. L., Juliano, T. J., Schneider, S. P., and Gronvall, J. E., "Hypersonic Boundary-Layer Transition Experiments in a Mach-6 Quiet Tunnel," AIAA Paper 2010-1061, January 2010.

[30]Kulite Semiconductor Products, Inc., *Pressure Transducer Handbook*.

[31]Schneider, S. P., "Development of Hypersonic Quiet Tunnels," *Journal of Spacecraft and Rockets*, Vol. 45, No. 4, July-August 2008, pp. 641–664.

[32]Chen, F.-J., Beckwith, I. E., and Theodore R. Creel, J., "Correlations of Supersonic Boundary-Layer Transition on Cones Including Effects of Large Axial Variations in Wind-Tunnel Noise," Technical Paper 2229, NASA, January 1984.

[33]Schneider, S. P. and Haven, C. E., "Quiet-Flow Ludwieg Tube for High-Speed Transition Research," *AIAA*, Vol. 33, No. 4, April 1995, pp. 688–693.

[34]Casper, K. M., *Hypersonic Wind-Tunnel Measurements of Boundary-Layer Pressure Fluctuations*, Master's Thesis, Purdue University School of Aeronautics & Astronautics, West Lafayette, IN, August 2009.

[35]Laderman, A. J., "Review of Wind-Tunnel Freestream Pressure Fluctuations," *AIAA*, Vol. 15, No. 4, 1977, pp. 605–608.

[36]Juliano, T. J., Swanson, E. O., and Schneider, S. P., "Transition Research and Improved Perfomance in the Boeing/AFOSR Mach-6 Quiet Tunnel," AIAA Paper 2007-535, January 2007.

[37]Schneider, S. P., Juliano, T. J., and Borg, M. P., "High-Reynolds-Number Laminar Flow in the Mach-6 Quiet-Flow Ludwieg Tube," AIAA Paper 2006-3056, June 2006.

[38]Balakumar, P. and Kegerise, M. A., "Receptivity of Hypersonic Boundary Layers over Straight and Flared Cones," AIAA Paper 2010-1065, January 2010.

[39]Li, F., Choudhari, M., Chang, C.-L., Wu, M., and Greene, P. T., "Development and Breakdown of Görtler Vortices in High Speed Boundary Layers," AIAA Paper 2010-705, January 2010.

[40]Saric, W. S. and Reed, H. L., "Supersonic Laminar Flow Control on Swept Wings Using Distributed Roughness," AIAA Paper 2010-0147, January 2002.

[41]Choudhari, M. M., Private Communication, February 2010, NASA Langley Research Center.